Università degli Studi di Padova

Sede amministrativa: Università degli studi di Padova
Dipartimento di Fisica "Galileo Galilei"
INFN - Laboratori Nazionali di Legnaro

SCUOLA DI DOTTORATO DI RICERCA IN FISICA
XX CICLO

Characterization of ALPI performances for future upgrades

Direttore della scuola: Ch.mo Prof. A. Stella

Supervisori:

Dott. A. Pisent

Ch.mo Prof. M. Pusterla

Candidato: Piero Antonio Posocco

31 luglio 2008

Contents

List of Figures

List of Tables

Preface

Introduction 1

1.1 AGATA requirements

1.2 SPES requirements

The PIAVE SC injector 2

The construction of a positive ion injector for the linac ALPI, named PIAVE, at Laboratori Nazionali di Legnaro was funded in 1996.

2.1 Scope of PIAVE

In 1996 the Legnaro accelerator complex consisted in a XTU tandem followed by the superconducting linear booster ALPI. It delivered ion beams to the experimental rooms with beam intensities on the target of few pnA, masses ranging from protons to masses of the order of 100 amu (^{81}Br) and energies well above the Coulomb barrier as it is shown in Fig. 2.1. The main constraint for the existing facility was the presence of the stripping section inside the tandem that limited the performance of the accelerator complex towards the heavier masses, up to 200 amu, and the beam intensities. On the other hand the nuclear physicists were moving their interests to the very heavy ion beams with energies around the interaction barrier.

As a consequence of this request a new injector for the ALPI booster had been proposed at the beginning of 1996. The injector PIAVE (Positive Ion Accelerator for Very low Energy) was meant for increasing the mass range of the facility up to lead ion. PIAVE uses the beams generated by the ECR Ion Source ALICE placed on a high voltage platform operated at 350 kV [1]. Figure 2.1 describes the performance of the tandem-ALPI complex and compares it with the foreseen capability of PIAVE in terms of specific energy of the beam versus the mass number. The values indicated near the curves are the beam currents on the target, in pnA, including a realistic transmission coefficient in ALPI of 50%. It clearly shows the possibility of reaching the heaviest masses keeping the energy of the beam above the Coulomb barrier and with beam currents on target more than adequate for nuclear physics experiments. The project had a three years time schedule and a cost of about 8 Billion Italian Liras.

2.2 PIAVE brief description

LEBT

The line, following the accelerating column, is composed by an achromatic bend, a couple of doublets that make a small waist at the buncher, followed by the second couple of doublets needed for the matching at the RFQ input. After the analysis of different options a three harmonics buncher was selected, with 40 MHz as fundamental frequency, at a distance of 3.51 m from the RFQ input. Indeed, since for each harmonic we use a two gaps configuration, the first and the third harmonics are applied in a first buncher, the second harmonic in a second buncher at a distance of 120 mm; all voltages are below 4 kV[4] [2]. The design efficiency of the bunching is such that 70 % of the particles are captured by the RFQ with a final RMS longitudinal emittance of 0.13 ns keV/u with nominal focusing. Simpler configurations, like double drift double frequency

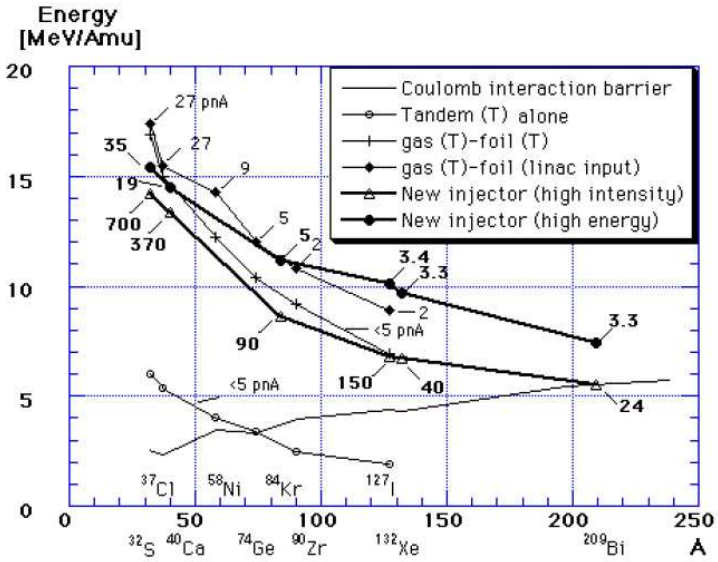

Figure 2.1: Performances of the Legnaro accelerator complex including the foreseen upgrading given by PIAVE [3].

bunchers, have not the same performances, due to the fixed distance between the two bunchers and the consequent difficulty of getting small beam waists in all gaps.

RFQ design characteristics

The heart of the new injector [5] (see Fig. **??**) is the superconducting RFQ section. The main design parameters are summarized in Tab. 1. The beam is pre-accelerated in a 312 kV platform and bunched with an external three harmonic buncher (40, 80, 120MHz) with the possibility of implementing a 5 MHz bunching system for TOF measurements later.

The SRFQ, without a complete bunching section, has been optimized to achieve a high accelerating gradient, since power losses are negligible and the cost of the structure and associated cryostat is rather high. This result has been obtained by splitting the RFQ in two independent cavities. In SRFQ2, thanks to the increased beta, both the intervane voltage V and the aperture R0 are almost doubled. In this second structure (with V = 280 kV) the accelerating field exceeds 2.8 MV/m, which is to our knowledge the world record for an RFQ, and the normalized transverse acceptance exceeds 2.5 mm mrad.

The two SRFQ resonators are of ladder kind, with four stems per electrode in SRFQ1 and two in SRFQ2; the transverse dimensions are therefore almost the same. The field configuration of the operating mode in these resonators is pretty insensitive to geometric errors, since in the worst case the resonator length is 0.37 λ and the dipoles are 10 MHz higher in frequency. It is instead very critical the tuning of the operating mode frequency (starting from an achieved mechanical accuracy better than 50 μm in the welded assembly) and the stiffening of the system against vibrations.

The physical distance between the two SRFQs (200 mm) determines a transverse beam mismatch in SRFQ2 (where the acceptance is large). This mismatch has been minimized interrupting SRFQ1 in a point where the Twiss parameter are $\alpha_x = \alpha_y = 0$. Longitudinally instead the phase advance is matched with the correct choice of the synchronous phase of SRFQ2. Moreover in the transition region we profit of an additional acceleration specific of these alternating stem structures [6].

Following the SRFQ (at beta=0.355) the beam enters directly the QWR section without a proper matching section. The longitudinal matching is here achieved using the first cavity

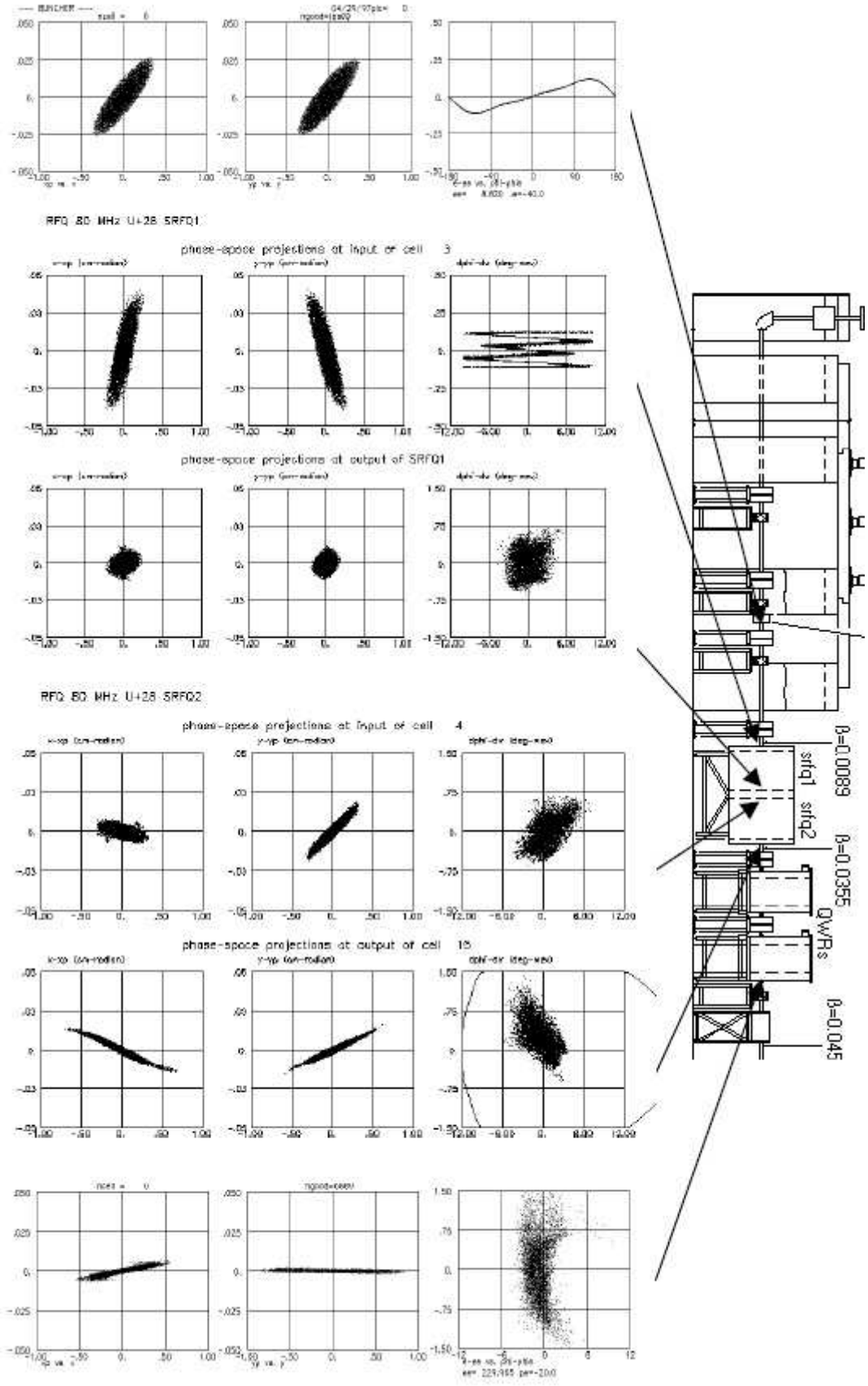

Figure 2.2: Piave original beam dynamics (1996) [**?**].

Table 2.1: Original Piave specifications.

parameter	base value		unit	comment
Source and LEBT				
Ion source	14.5		GHz	ECRIS
max A/q	8.5			for $^{238}U^{28+}$
max platform voltage	315		kV	
rms emittance	0.1		mm mrad	normalized
bunching system	40; 80; 120		MHz	three harmonics
$\Delta\phi$	± 6		deg	@ 80 MHz
ΔW	± 0.55		keV/A	
RFQ Accelerator				
Radio Frequency	80		MHz	
input energy	37.1		keV/A	β = 0.0089
output energy	586		keV/A	β = 0.0355
max surface field	25		MV/m	
max stored energy	≤ 4		J	each RFQ
acceptance	≤ 0.9		mm mrad	normalized
output emittance rms	0.1		mm mrad	normalized
	≤ 0.14		ns keV/A	
	SRFQ1	*SRFQ2*		
Vanes length	137.8	74.61	cm	
Output energy	341.7	586	keV/A	
max voltage	148	280	kV	
number of cells	42.6	12.4		
average aperture R0	0.8	1.53	cm	
modulation factor m	1.2-3	3		
synchronous phase	-40 ÷ -18	-12	deg	
QWR section				
number of resonators	8			
output energy	948		keV/A	β = 0.045
radio fequency	80		MHz	
optimum β	0.05			
accelerating field	3		MV/m	
shunt impedance	3.2		kΩ/m	
synchronous phase	-20		deg	
Matching line to ALPI				
number of bunchers	2			room temperature
buncher eff. voltage	≤100		kV	VT

as a buncher, and with alternating phase focusing. The synchronous phase sequence is (-90, +20, +20, +20, -20, -20, +20, +20). This approach allows a compact system, but is sensitive to alignment errors that can easily result in important longitudinal emittance increase. Finally the beam is transported into ALPI super-conducting linac through a 90ř achromatic bending and longitudinally matched with two normal-conducting QWR bunchers.

2.3 Longitudinal emittance measurements

Longitudinal emittance has also been measured in the same position, using a silicon detector intercepting the particles scattered at 250 angle by a thin golden foil. The data acquisition system allows to determine the time-energy correlations with the possibility (in principle) to get a direct plot of the longitudinal emittance. In practice, while the bunch length measured seems correct, we have not yet been able to get an acceptable energy resolution. The comparison of the energy spread of an Ar beam after the RFQ as foreseen by simulations, as measured with silicon detector and as measured with magnetic dispersion after the dipole PD3 indicates that the silicon detector overestimates of an order of magnitude the energy spread. The spread from simulation is $\Delta W/W = 0.3$ %, while Si measurement gives $\Delta W/W = 9.0$ % and magnetic dispersion $\Delta W/W = 0.6$ %.

As a consequence the rms emittances measured with time-energy correlation of Si detector signals are overestimated. We have therefore decided to measure the longitudinal emittance indirectly, following the three gradients method, changing the field of the third QWR cavity, used as a buncher with $\phi_s = -90^0$. The computed emittances are reported in Tab. 3. The three gradients method instead gives an emittance value that is within a factor 2.5 in agreement with what expected from simulations for a perfectly aligned machine. This result is encouraging and shows that the SRFQ can give a longitudinal emittance perfectly comparable with the performances of the other heavy ion injectors.

The transfer matrix for the longitudinal plane between the SRFQ out and the emittance-meter is

$$R_z(VT) = \begin{pmatrix} 1 & L_2 \\ 0 & 1 \end{pmatrix} \begin{pmatrix} 1 & 0 \\ 0 & k_z\, VT \end{pmatrix} \begin{pmatrix} 1 & L_1 \\ 0 & 1 \end{pmatrix},$$

where $L1 = 1.9$ m and $L2 = 5$ m. In between there is the accelerating cavity QWR03-1 which act as buncher (synchronous phase set to -90 deg and accelerating field lower than 0.5 MV/m).

In order to calculate both the Twiss parameter and the rms emittance at SRFQ output we just need to know the dependence of the squared rms phase width on the equivalent voltage VT of the cavity[1]. In facts, the longitudinal σ matrix of the beam at one place is

$$\sigma(\alpha_z, \beta_z, \varepsilon_z) = \begin{pmatrix} \beta_z\, \varepsilon_z & -\alpha_z\, \varepsilon_z \\ -\alpha_z\, \varepsilon_z & \frac{1+\alpha_z^2}{\beta_z}\, \varepsilon_z \end{pmatrix},$$

and therefore $\sigma_{1,1} = \sqrt{\beta_z\, \varepsilon_z} = \phi_{rms}$.

We have to transport the beam from the emittance-meter backwards to the SRFQ output in this way

$$\sigma'(\alpha_z, \beta_z, \varepsilon_z) = T^{-1} \cdot R_z(VT) \cdot (T \cdot \sigma(\alpha_z, \beta_z, \varepsilon_z) \cdot T) \cdot R_z(VT)^T \cdot T^{-1}$$

where

$$T = \begin{pmatrix} -\frac{\beta\, \lambda}{360} & 0 \\ 0 & -\frac{\gamma}{(\gamma+1)\, E\, 1000} \end{pmatrix}$$

is the matrix which converts the longitudinal σ matrix in MeV deg units to mm mrad units.

[1] $VT = TTF \cdot E_{acc} \cdot L_{eff}$.

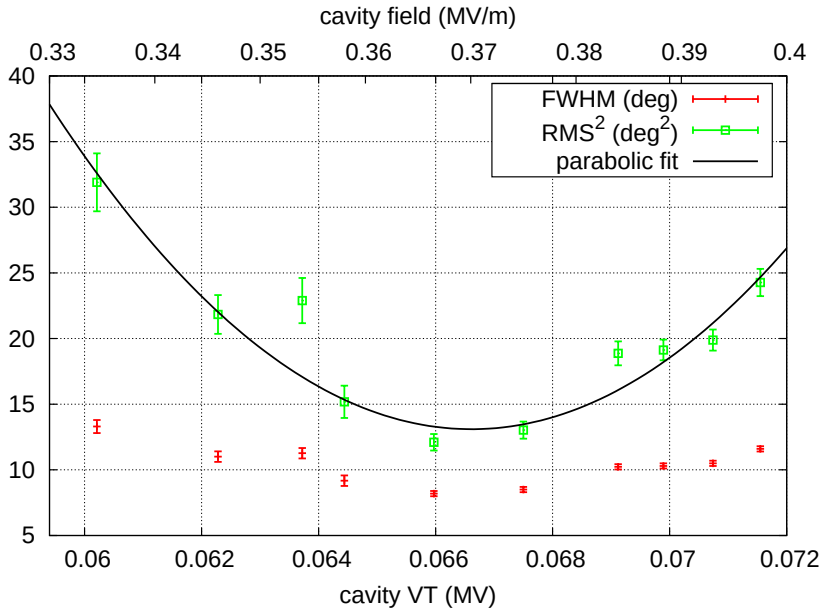

Figure 2.3: Longitudinal emittance measurements out of PIAVE SRFQ.

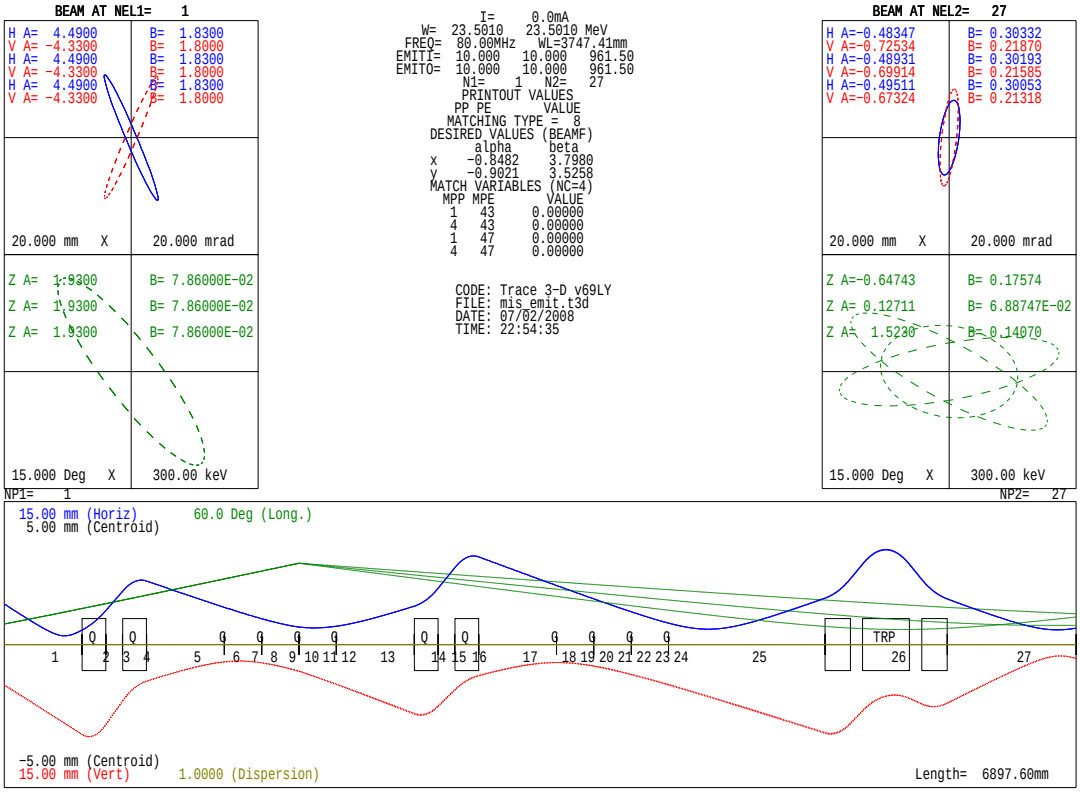

Figure 2.4: Trace3D 3 gradient longitudinal emittance plot for $VT = 0.6$ MV, $VT = 0.66$ MV (minimum) and $VT = 0.72$ MV.

Table 2.2: The parabola fitting parameters for the three gradient method.

fit parameters	value	rel. error
$\varepsilon_z\ a\ (\alpha_z, \beta_z)$	$(47.5 \pm 6.9) \times 10^4$	15 %
$\varepsilon_z\ b\ (\alpha_z, \beta_z)$	$(-63.3 \pm 9.2) \times 10^3$	15 %
$\varepsilon_z\ c\ (\alpha_z, \beta_z)$	$(21.2 \pm 3.2) \times 10^2$	15 %

Now, since $\sigma_{1,1}$ results to be a quadratic function of VT,

$$\sigma_{1,1} = \varepsilon_z \cdot (a\ (\alpha_z, \beta_z)\ VT^2 + b\ (\alpha_z, \beta_z)\ VT + c\ (\alpha_z, \beta_z))$$

we have to fit the squared rms phase data (the data acquisition was made via FWHM phase then converted to RMS as explained in Sec. B.1) obtained spanning the VT around the minimum of the phase. The parabola parameters obtained by the fit are reported in Tab. 2.2.

Hence the Twiss parameter are calculated numerically inverting the system and the results are reported in Tab. 2.3.

Table 2.3: Longitudinal beam parameters out of PIAVE SRFQ.

long. parameters	value	unit	rel. error
α_z	1.93 ± 0.15		7.8 %
β_z	3.14 ± 0.16	deg / MeV / A @ 80 MHz	5.3 %
ε_z	4.81 ± 0.22	deg MeV / A @ 80 MHz	4.5 %

Bibliography

[1] M. Cavenago and G. Bisoffi, *Commissioning of the ECR ion source Alice*, NIM **A328** (1993), no. 193, 262–265.

[2] M. Comunian and A. Pisent, *LEBT and three harmonics buncher design for PIAVE*, LNL Annual Report 1996 (Legnaro (PD), Italy), INFN, 1996.

[3] A. Lombardi et al., *The new positive ion injector PIAVE at LNL*, Proceedings of PAC97 (Vancouver, Canada), IEEE, 1997, pp. 1129–1131.

[4] A. Facco and F. Scarpa, *The new triple harmonic buncher for the PIAVE project*, LNL Annual Report 1996 (Legnaro (PD), Italy), INFN, 1996.

[5] A. Pisent, Proceedings of the 8th HIAT International Conference, no. 473, 1998, p. 214.

[6] A. Pisent and M. Comunian, *Complete simulation of the heavy ion linac PIAVE*, Proceedings of PAC97 (Vancouver, Canada), IEEE, 1997, pp. 1132–1134.

The ALPI SC boostr 3

3.1 ALPI Project

The ALPI project [1] started in 1989 with the primary goal of extending the XTU tandem performance toward heavier beams and higher energies due to the demands of nuclear physics experiments. Since the very beginning the project adopted the philosophy of basing the acceleration on independently phased super-conducting quarter wave resonators (QWR) and following the Argonne National Laboratories it carried out the idea of installing a positive ion injector (PIAVE) in order to substantially improve the beam intensity of medium-heavy ion species.

3.1.1 ALPI accelerator description

At the time of project beginning Lead plating technology was the most straightforward choice for ALPI linac as far as time and cost saving were concerned but a long term research plan immediately started aiming at the fabrication of niobium-based QWRs with performance in excess of 5 MV/m at 7 W of power dissipation [2]. In particular, a new sputtering laboratory was set up and recently resonators with a Q-performance as high as 7 X lo have been produced employing the dc biased diode technique [3].

The two main peculiarities of our linac are:

- the oversimplified inner conductor geometry of our QWRs [4]
- the beam transport philosophy which is based upon the possibility of frequent (every second cryostat) beam diagnostics [S]

The open end of the inner conductor, shaped like a hemisphere, is particularly convenient as far as the machining and the sputtering processes are concerned. Moreover, it has been shown that such a resonator exhibits negligible dipole and quadrupole field components in the velocity range which maintains an optimum accelerating field. The accelerating part of the linac configuration (see Fig. 3.2) consists of 11 modules (fsee Fig. 3.1) each consisting of two cryostats, one diagnostics box, one focussing Q-triplet and two steerers. While the basic architecture of the machine module has remained constant for a long time, some modifications with respect to the original design have been introduced in the injection and return lines (the return line connects the linac to the target halls through the present switching magnet). The two lines, which are inclined at - 6’ with respect to the horizontal plane because of the displacement of 4 m between the tandem and the linac floor, behave as fully isochronized beam transport systems. While the isochronism in the injection lines is accomplished by creating a cross-over midway between the two dipoles ID1 and ID2 (two Q-doublets and one Q-singlet are inserted between ID1 and ID2), in the return line the goal is reached by putting two 7’ bending dipoles in an S-configuration and letting the beam cross inside them.

In order to manipulate the longitudinal phase space conditions of the beam according to experimental requirements, two bunching/debunching resonators will be used in the return line.

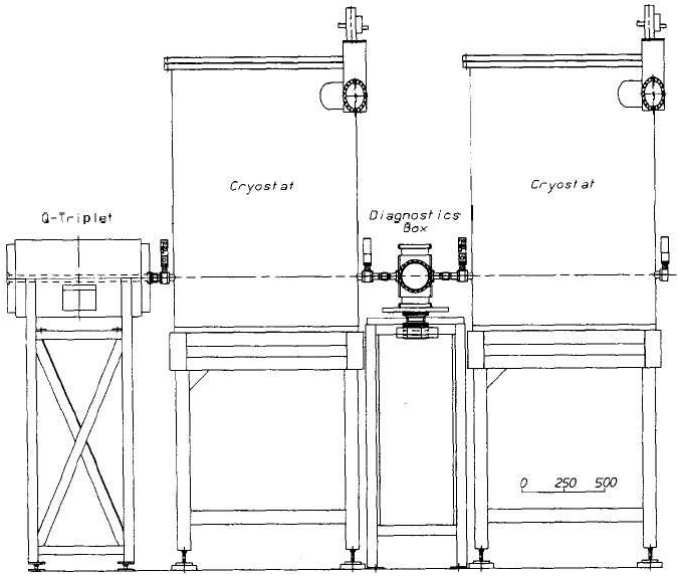

Figure 3.1: Basic module of the linac.

In the final design their locations have been changed; the one (160 MHz superconducting QWR) originally foreseen at the midpoint of the S-bend has now been moved 0.5 m upstream of the first 7" bending dipole, while the position of the other (160 MHz room temperature re-entrant cavity), previously placed in front of the switching magnet, has been shifted 0.5 m downstream of the second 7" bending dipole. In this return line reconfiguration, which is based upon an improved handling of the longitudinal phase space ellipse (the beam in the S-bend is transported almost completely debunched), we avoid both the special 17 m long helium distribution line feeding the buncher cryostat being placed 2 m higher than all the others and the necessity to keep the cryostat itself tilted at 7" with respect to the usual vertical position. In a test run with a Ni beam aiming at checking the alignment accuracy of the injection line, we did not face any serious problem apart from the steering effect introduced by the tandem analyzing magnet residual field. Once this effect is properly compensated, the beam is correctly transported throughout the injection line provided that the beam cross-section is round at the ID1 object slits and the two beam profile monitors placed symmetrically apart with respect to the midway cross-over show the same beam profile. 2. Status of the project Initially, the ALPI project was scheduled in two temporally distinct phases according to the user needs of having in a short time a machine with beam energy performance similar to that of a 35 MV tandem for ion species as heavy as 100 amu. All the auxiliary equipment was dimensioned accordingly in order to keep the medium section of the linac (48 QWRs with P = 0.11) running during the first phase. However, with the aim of reducing costs and simplifying machine assembly, the plan was significantly changed during its execution and most of the infrastructures and plants are now already prepared for the final phase.

3.2 Experience with ALPI accelerator

Bibliography

[1] G. Fortuna et al., NIM **A287** (1990), 253.

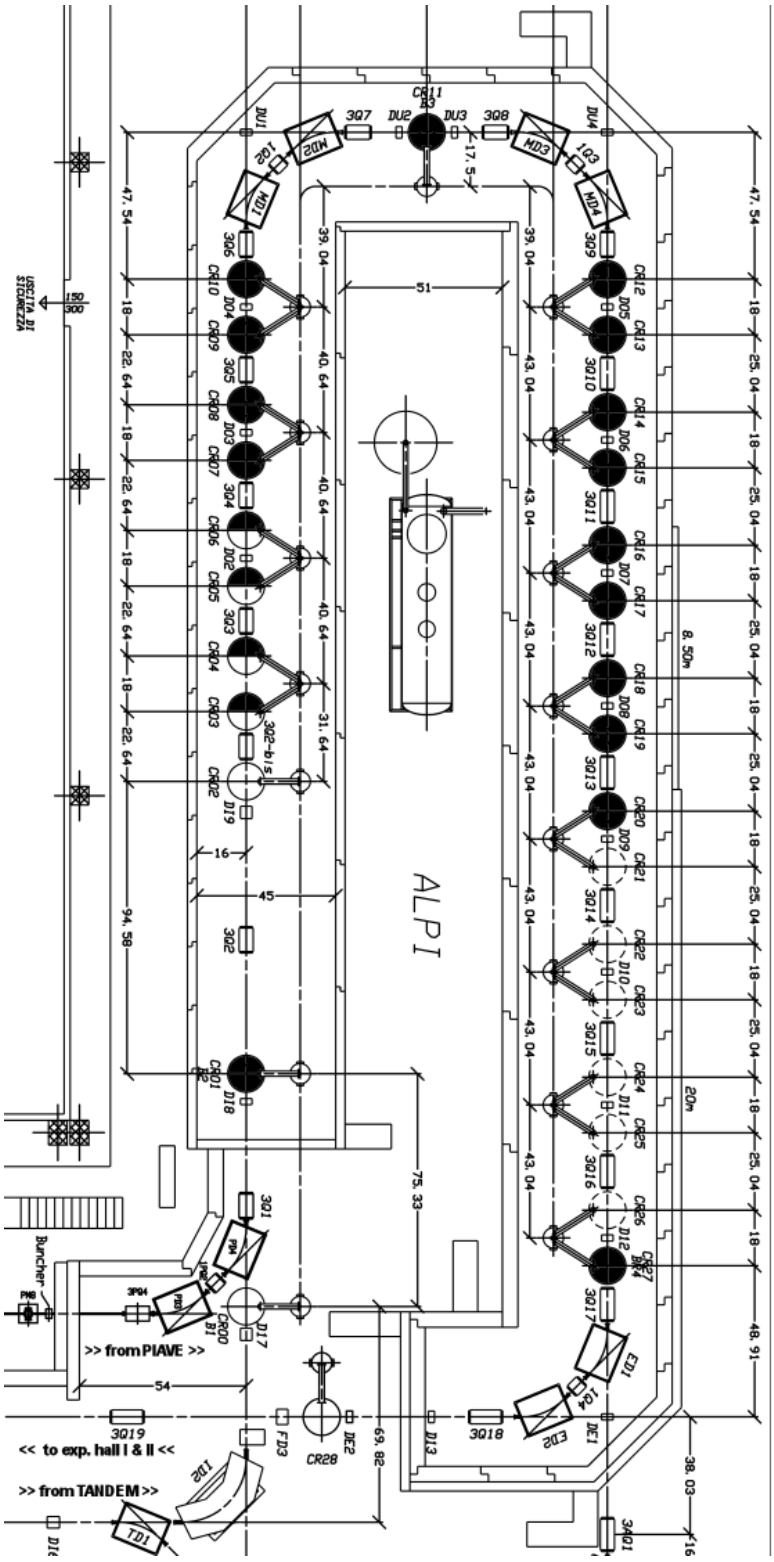

Figure 3.2: ALPI map. The full black circles represent the 160 MHz QWRs and the half black ones the 80 MHz QWRs.

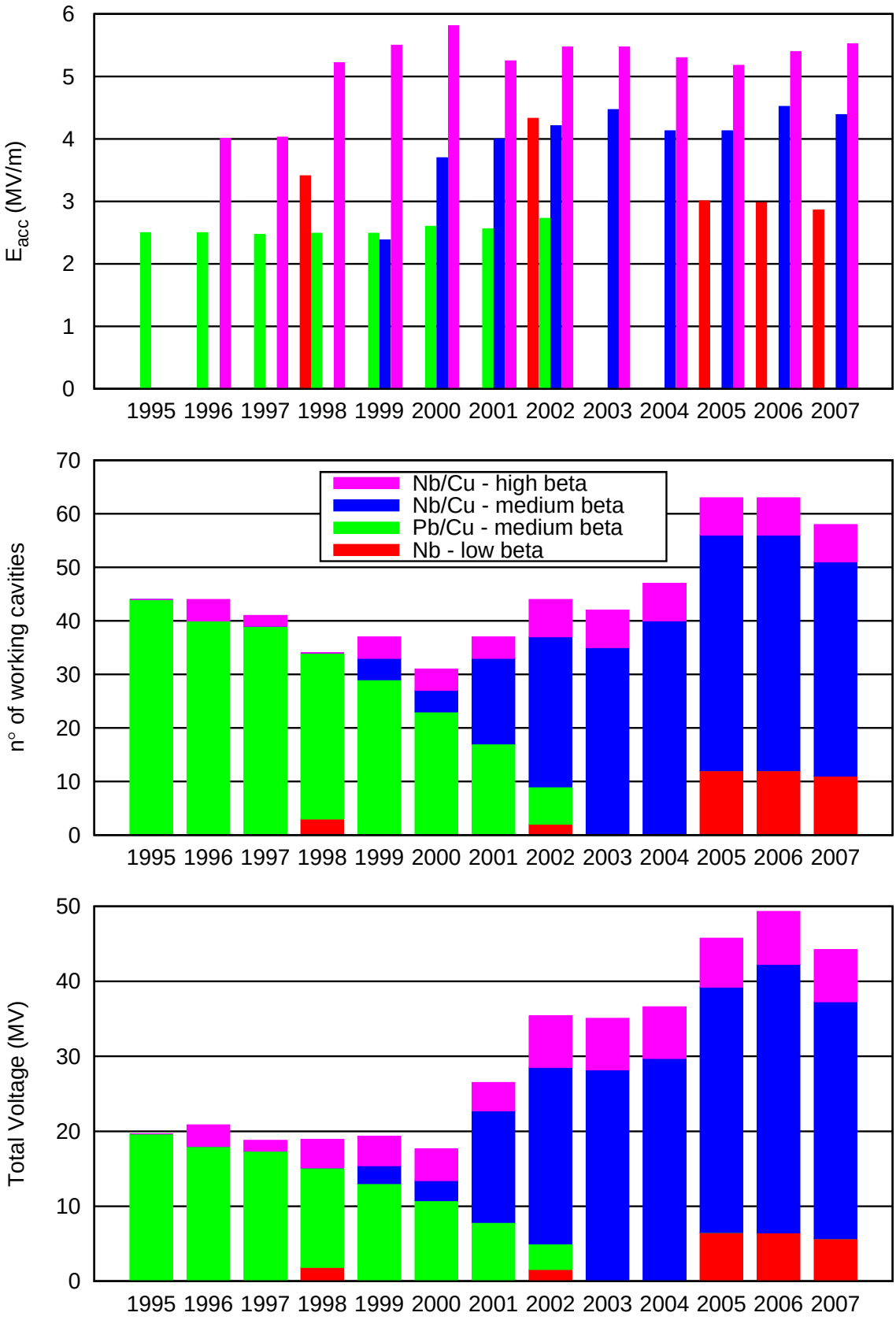

Figure 3.3: ALPI QWR performances since 1995.

The acceptance tests for the new Legnaro ECRIS

4

The PIAVE injector has regularly worked since 2001. After a first period of accelerator commissioning in 2006 the beams coming from PIAVE are in the regular beam time schedule. The ALICE ion source, core of PIAVE injector, is now 15 years old. More than one generation of ECR ion sources have been developed in the meantime, offering far better performances in terms of extracted beam current in simpler designs. The ECR ions sources are so widely use that, even if they still continue to be part of interesting research and technology programs, they have become a standard product on the accelerator technology market. Two years ago the Legnaro National Laboratories decided to buy a new ion source to replace the old ALICE and the choice fall on a product of the French company Pantechnik, the Supernanogun.

4.1 ECRIS: brief introduction

Several general characteristics of ECR sources explain their widespread application in the accelerator community. Most important is the ability to produce CW beams from any element at useful intensities for nuclear and atomic physics research. Another characteristic of ECR sources is that the discharge is produced without cathodes. Therefore, only the source material injected into an ECR source is consumed. As a result, ECR sources can be operated continuously for long periods without interruption. Maintenance required on ECR sources is also minimal, consisting mainly of occasional repair of vacuum equipment, external ovens and electrical support equipment.

4.1.1 ECRIS characteristics

An ECR Ion Source (ECRIS from now on) consists of a vacuum chamber working as resonant cavity for microwaves (usually from 14-18 GHz), multiple solenoids for axial magnetic confinement, a multipole magnet (usually a sextupole) for radial confinement and an extraction system made usually of three electrodes for ion beam production. The microwaves could be coupled to the source both on and off axis, via rectangular waveguides: they deliver the electromagnetic radiation which heats electrons through a process called Electron Cyclotron Resonance (ECR). The plasma electrons have two components, a cold population (~20 eV) and a hot population that has a high energy tail reaching up to 100 keV or more. Typical ion energies are a few eV. The electrons produce the high charge state ions primarily by sequential impact ionization. The ions and the electrons must be confined for sufficient time for the sequential ionization to take place. In a typical ECRIS, the ion confinement times need to be about 10^{-2} s to produce high charge state ions. The ionization rate depends on the plasma density, which typically ranges from about 10^{11} cm^{-3} for low frequency sources to more that 10^{12} cm^{-3} for the highest frequency sources. Charge exchange with neutral atoms must be minimized, so operating pressures are typically 10^{-6} Torr or less. The plasma chamber is biased positively so that at extraction the ions can be accelerated out of the plasma and into the beam transport system.
The following sections will briefly explain most of the topics related with ECRIS.

Electron Impact Ionization. In ECR sources multiply charged ions are created mainly by step-by-step ionization, caused by the successive impact of energetic electrons. Therefore the electron impact ionization cross sections are significant parameters.

Charge Exchange. Two processes dominate the loss of high charge state heavy ions from the plasma. These are charge exchange with neutral atoms in the plasma and loss of confinement. The cross sections for charge exchange between highly charged ions and neutrals are extremely large. Typical charge exchange cross sections are three to four orders of magnitude larger than corresponding electron impact ionization cross sections. Fortunately, the reaction rates are proportional to the projectile velocities, and neutral atoms are much slower than hot electrons. Still, to keep the rate of production by electron impact equal to the rate of loss by charge exchange for high charge state ions, it is necessary for the neutral atom density in the plasma to be two orders of magnitude lower than the electron density.

Plasma confinement. The processes that govern particle confinement in an ECRIS are complex. The temperatures of electrons and ions are different and their confinement times vary considerably. Furthermore, the electron velocity distribution function consists of more than one population, usually described as cold, warm, and hot populations. Since the confinement times are proportional to the electron temperatures, they are different for each electron population. The ion confinement time is naturally a very critical parameter in ECRIS, where it is not possible to arbitrarily interrupt the ion confinement to extract the confined ions. However, if this confinement time is too short, ions do not have time to reach high charge states and if the confinement time is too long, the high charge state ions decay by charge exchange instead of being extracted as a useable beam. To improve the confinement of the ECR plasma, turbulence should be avoided. As a result, there is a maximum power density for each ECR source that can be coupled in and a maximum plasma density (typically lower than the cut-off frequency) that can be achieved before plasma instabilities begin to decrease the high charge state performance. These limits increase with frequency and magnetic field strength.

Particles, which oscillate back and forth in the magnetic mirror, can be scattered into the loss cone by collisions. Thus the confinement time for ions is related to the scattering rate for ion-ion collisions and the confinement time for electrons is related to the scattering rate for electron-ion collisions. For particles to be magnetically confined, the rate for scattering through a large angle must be small compared to their gyro frequency in the magnetic field. High energy electrons, which have low collision rates, are well confined. The warm electrons suffer more frequent scattering collisions and are less well confined. On the other hand, the ions are highly collisional and are therefore not magnetically confined. For high charge state ECR ion sources, simple axial mirrors do not provide sufficient magnetic confinement. In addition to the axial magnetic field produced by solenoids, the typical high charge state ECR source uses a sextupole (also called hexapole) or other multipole magnet to produce a radially-increasing field. The combination of the axial mirror field and the radial multipole field produces a "minimum-B" magnetic field configuration, where the magnetic field is a minimum at the center of the device and increases in every direction away from the center. Such a field provides a plasma confinement geometry that is stable against MHD instabilities. The ratio of the maximum field strength at the peak of the magnetic mirrors to the minimum field strength at the center of the device is defined as the axial mirror ratio, $R_m = B_{max}/B_{min}$. The ratio of the minimum field at the center of the plasma chamber to the maximum field at the plasma chamber wall (moving radially at midplane) defines the radial mirror ratio. While the early ECR ion sources operated with axial and radial mirror ratios with values less than two, the newer sources use mirror ratios as high as 4 at injection, 2 at extraction, and slightly greater than 2 in the radial direction. These higher mirror ratios improve the plasma confinement and this shifts the charge state distribution to a higher average charge.

ECR heating. To optimize the rate of ionization by electron impact, electron temperatures be-

tween 1 keV and 20 keV are typically needed. The ion temperature on the other hand should be as low as possible because the ion temperature is one source of emittance and energy spread of the extracted beam. Therefore, a method to selectively heat the electrons in the plasma is desirable. The use of ECRH meets this requirement. If we introduce into the plasma an electromagnetic wave, whose frequency is equal to the cyclotron frequency of the electrons in the magnetic field, an extremely efficient energy transfer occurs between the wave and the electron population. In a minimum-B configuration, the magnetic field is not uniform but increases from the center to the outside. Therefore the ECR condition is normally met only on a closed surface around the center, called the "ECR surface", which must be closed inside the plasma chamber. For high performance ECR ion sources, the ECR surface sits well inside of the plasma chamber wall, which means high radial confinement performances.
In a simplified picture, the plasma can be described as a high-pass filter for microwaves propagation. Microwaves with frequencies higher than a critical frequency, called the plasma frequency, can propagate while microwaves with frequencies lower than the plasma frequency are reflected. The plasma frequency, f_p, is a function of the plasma density,

$$f_p = \frac{1}{2\,\pi}\,\sqrt{\frac{n_e\,e^2}{\epsilon_0\,m_e}}, \tag{4.1}$$

where n_e is the electron density, e is the electron charge, m_e is the electron mass, and ϵ_0 is the permittivity of free space.
For a given microwave frequency, f_{rf}, the critical density, n_{crit}, is defined as the density for which f_p equals f_{rf}. Rewriting Eq. 4.1 in practical units gives the critical density in terms of the microwave frequency as

$$n_{crit} = 1.26 \times 10^{-8} f_{rf}^2, \tag{4.2}$$

where now n_{crit} is in units of electrons/cm^3 and f_{rf} is the microwave frequency in Hz.
The critical density is an upper bound on the useful plasma density that can be achieved in high charge state ECR ion sources.Measurements of plasma densities in ECR ion sources have show that the hot electron population makes up roughly 10% of the total electron density, which can be close to the critical density. Therefore, the use of higher frequencies seems the only practical way to reach higher plasma densities in ECR sources. Low frequency ECR ion sources operate at 2.45 GHz where the critical density is 7.6×10^{10} cm^{-3}, many sources now operate at 14.5 GHz (like the ECRIS operating at LNL) or 18 GHz where the critical densities are 2.7×10^{12} and 4.1×10^{12} cm^{-3}, and sources operating at 28 GHz are being developed where the critical density is 9.9×10^{12} cm^{-3}.

Gas mixing. It was discovered during operation of ECR sources that the production of high charge state ions can be substantially enhanced by adding a light support or mixing gas (typically oxygen) to the ECR plasma. Normally about 80% mixing gas is used and it can be up to 95% or higher for very heavy elements. However, a too high ratio of mixing gas increases the neutral pressure inside the ECR plasma and may also limit the production of higher charge states and the maximum intensity of heavier ions. A widely accepted explanation of this effect is that energy is transferred in collisions between the lighter mixing gas ions and the heavier ions, which cools the heavier ions and increases their confinement time. In addition, the lighter ion also lowers the average charge of the plasma, which again increases the plasma confinement time.

4.1.2 Beam production

ECRIS can in principle ionize each atomic specie in gaseous form: typical gaseous beams are O^{6+}, Ar^{9+}, Xe^{26+}. C^{4+} is now widely used in facilities for hadron therapy like CNAO in Pavia [2].
For those atomic species which are not gaseous at room temperature, different methods can be used to vaporize and then ionize such species:

Resistive oven Of all the methods for the production of metal ion beams, the oven technique is the least intrusive, especially if pure metals can be used. Generally, a metal vapor pressure of about 10^{-3} to 10^{-2} Torr is required inside the oven (for an oven aperture of about 3 mm diameter) to supply the right amount of atomic flux to the ECR plasma. The temperature needed to produce a particular metal ion beam can be estimated from the vapor pressure curve of the metal. Besides the temperature required to evaporate the metal, chemical compatibility of the hot liquid metal and the crucible must be considered. For metals with temperature requirements less than 1600 C ceramic inserts such as zirconia, alumina or yttria can be used to prevent alloying of the heating crucible with the molten metal. For higher temperatures, ceramics begin to sublime and can even react with the hot metals. Therefore, the material has to be either loaded directly into the W or Ta furnace or special crucibles must be used.

RF oven. [3].

Sputtering system. For the sputtering technique, a sample is mounted radially at the periphery of the plasma and is negatively biased with respect to the plasma. The sample is sputtered by the plasma ions, and neutral metal atoms diffuse into the ECR plasma where they are ionized. This technique partly decouples the ECR plasma from the evaporation process. However, adequate plasma density is required to ensure sufficient sputtering rate, and therefore the ion source tuning is not completely decoupled from the evaporation process. Furthermore, the achievable intensities are dependent on the sputtering yield. Thus the sputtering method is very convenient for low intensities, but has limitation for the production of high intensity metal beams.

Direct insertion. The direct insertion technique was one of the first to be utilized for a wide variety of metals and is still used by most ECR groups. A support gas such as oxygen sustains the plasma while a solid rod is positioned close to the plasma, where it is vaporized and the vapor is subsequently ionized. Though the insertion technique is simple and effective, it has the operational disadvantage of strong coupling between plasma and sample heating. However, for some refractory metals (e.g., tantalum) it may be the only choice available. Stable operation can be achieved by carefully controlling the position of the rod.

MIVOC. In some cases, gaseous compounds can be used, especially if the components of the compound can serve as a good mixing gas. Generally, one has to look for compounds with light elements. Sulfur for example can easily be produced from SO2, CS2 or H2S. Oxygen is an excellent mixing gas, therefore a compound containing oxygen is best choice if the desired metal is heavier. If the desired metal is lighter than oxygen, hydrogen is the better choice. Carbon contaminates the plasma chamber walls and should be avoided whenever possible. The metallic compound is loaded into an external chamber and connected to the source by a leak valve. After the initial pump down of the residual gas in the MIVOC chamber, the compound vapor can be introduced into the source as an ordinary gas. The main advantage is the fast setup time and ease of use, but rare isotopes are often not readily available in the appropriate chemical form. Another major drawback is the impurities (in particular carbon, e.g. ten carbon atoms for one Fe atom), which contaminate the plasma chamber walls. The ion source performance and stability can be compromised, particularly for long duration, high intensity applications.

4.1.3 Beam extraction

4.2 The PIAVE ion source upgrade

From the previous sections it comes out that the sensitive parameters of ECRIS are the maximum confinement magnetic field B and the RF frequency f. In particular three empirical laws [1]

Table 4.1: Supernanogan guaranteed intensities (μA). The cells in gray represent the beams and charge states among the guaranteed ones chosen for the acceptance test.

	1+	2+	4+	6+	8+	9+	11+	14+	20+	23+	25+	26+	27+	30+
H	2000													
^{2}H	2000													
^{3}H	700													
He	2000	1000												
C	500	350	200	3										
N	1000	300	100	10										
O	1000	400	300	200										
Ne	1000	300	200	160	25									
Ar	1000	350	250	200	200	90	30	1						
Kr	1000						25	15						
Ag			250	250	200	90	30		4					
Xe	500				220				15	14	10	5		
Ta									4	0.8				
Au												10	6	1
Pb									10			3	1	

Table 4.2: Alice and LEGIS comparison table. The new LEGIS represents a step forward in terms of charge states availability and beam current.

	Alice	LEGIS
microwave frequency	14.5 GHz	14.5 GHz
max. microwave power	350 W	700 W
axial field	up to 0.8 T	1.1 T
radial field at chamber wall	0.7 T	0.9 T
maximum extraction voltage	12 kV	30 kV
Ag	0.87 μA ($^{19+}$)	4 μA ($^{20+}$)
Ar^{9+}	10 μA	100 μA
Xe^{23+}	1 μA	14 μA

describe how the performances in terms of charge state production and intensity are effected by the source design parameters:

$$q_{opt} \propto \log B^{3/2}, \qquad q_{opt} \propto \log f^{7/2} \qquad \text{and} \qquad I^{q+} \propto f^2,$$

where q_{opt} is the peak of the charge state distribution and I^{q+} is the current of the selected charge state. On the other hand the extracted current is proportional to the RF power.
Keeping the RF frequency fixed, better performances are obtained increasing the confinement magnetic field and RF power. Looking at the comparison table (Tab. 4.2) it is clear that the Supernanogan has far better performances. The noble gases are 10 times more intense and the example of a resistive oven ionized specie shows a factor of 4. To allows a higher maximum extracted current the extraction voltage is higher as well as the microwave power and the confinement field.

To be sure that the higher current is not obtained to the detriment of beam emittance (as reported in Tab. 2.1 the acceptance of the PIAVE SRFQs is less than 0.9 mm mrad norm.) a proof of the beam quality was required.

4.3 LEGIS acceptance tests

4.3.1 LNL requests by contract

y contract a beam current stability two-hours test was required. During the test the current read by the Faraday cup had to stay within ± 5 % of the currents reported in Fig. 4.3 except for maximum 2 % of the time (less than 4 mins). The operator could tune the source to recovery the current after a blackout or to increase its stability during the test for a maximum of 15 mins. An additional specification on beam quality was required for O^{6+} and Ar^{9+} ion beams: the measured normalized rms emittance for 90 % of the beam had to be lower than 0.3 mm mrad. The emittance measurements were carried out for Au^{26+} beam as well.

Table 4.3: Supernanogun LNL requested performances by contract.

beam	ion	I (μA)
gaseous	O^{6+}	200
	Ar^{9+}	100
metallic from sputtering	Ta^{24+}	1
metallic from oven	Ag^{21+}	3
	Au^{26+}	10
	Au^{30+}	1

The gaseous beams chosen for the test are the easiest beams which the source can provide and therefore they will be the first extracted beams once the source is installed on the platform at LNL. The O^{6+} beam has been also the primary beam used for PIAVE commissioning. Ta^{24+} is the only metallic beam generated via sputtering on the Supernanogun guaranteed beams list. The tests on the metallic beams from oven are very important to check the performances of the oven itself. The reason of three kind of beams is evident: Ag^{21+} is a medium mass easy to vaporize beam, Au is a heavy beam with a 500 C higher boiling point and with an ionized q/A which gives 7.6 for 26+ and 6.6 for 30+, where only the latter could work for the ALPI upgrade described in this thesis.

4.3.2 The LNL test bench at Pantechnik

The LEGIS test bench at Pantechnik comprises:

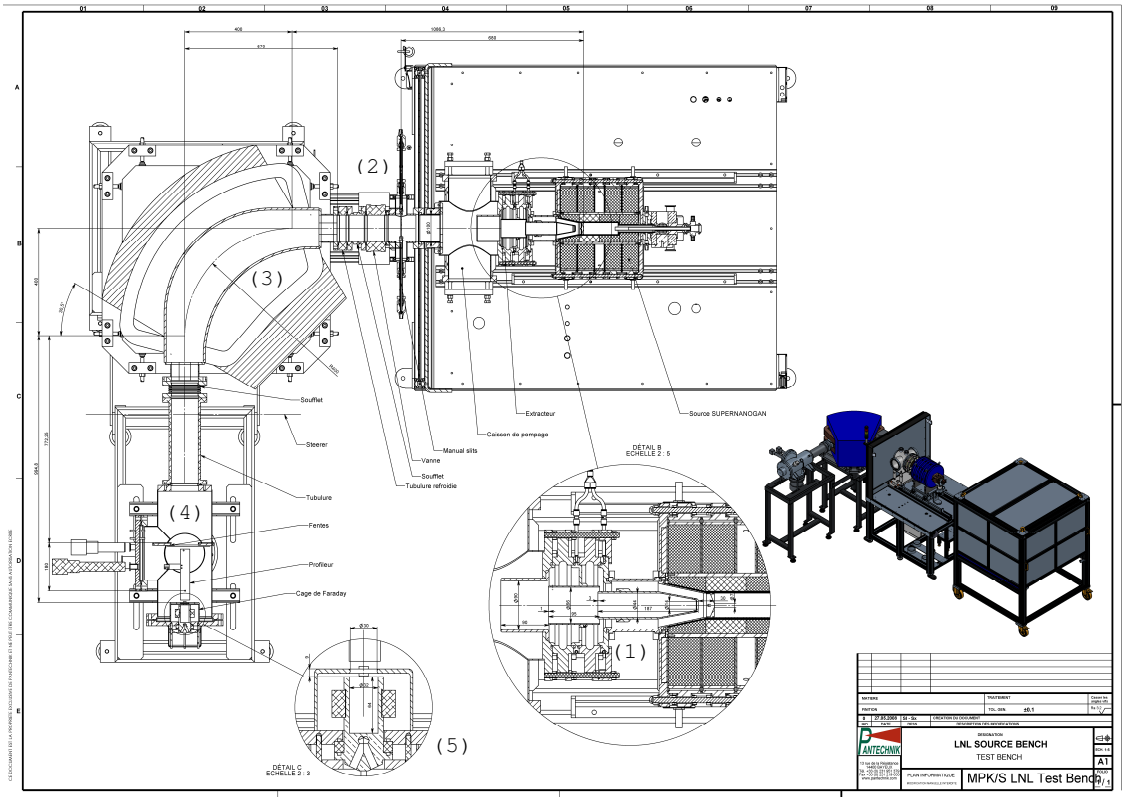

Figure 4.1: The LNL test bench at Pantechnik company. (1) extraction system, (2) slits, (3) analysis dipole, (4) emittance-meter and (5) Faraday cup.

Table 4.4: Pantechnik test bench details.

extraction gap (mm)	30
dipole edges (deg)	30.5
plasma electrod to dipole (mm)	1120.6
plasma electrod to slit (mm)	704.8
dipole to slit (mm)	780
slit to wire (mm)	180
dipole to Farady Cup (mm)	1002.6
slit step = slit width (mm)	0.5
wire step (mm)	0.25

Table 4.5: LEGIS source settings during the test.

	Ar^{9+}	O^{6+}	Ta^{24+}	Ag^{24+}	Au^{26+}	Au^{30+}
puller voltage (V)	0	-210	-371		-385	-582
lens voltage (V)	922	882	875		948	1040
power (W)	166	177	177		444	384
total extracted current (mA)	3.2	4.6	1.8		3.37	3.2
Bias voltage (V)	-382	-368	546		-558	-469
Bias current (mA)	1.47	2.20	2.39		1.32	1.15
slit diameter (mm)	28	30			12	12

1. the ion source and the 4 electrodes extraction system (plasma electrode, puller, focussing lens to analysis dipole and ground electrode);
2. the slits placed after the extraction system which cut the external part of the beam. In such a way the total transported current diminishes but the beam selected by the dipole has better emittance for a given current (preliminary tests by Pantechnik);
3. the analysis dipole, 90 degree bend and 400 mm radius;
4. the emittance-meter consisting of a variable slit and a independently moving wire. The control system provides the step value, the slit dimensions (which are set equal to intercept the entire beam without overlapping) and the wire sampling points number. The slits are used to increase the A/q resolution as well.
5. the Faraday cup, 30 mm diameter.

The extraction voltage was set to 24 kV for all the extracted beam. In Tab. 4.4 all the main characteristics for beam optics are reported. This test bench represents at its best the situation on PIAVE platform so to make easier the first tests on-site. The set-up of the emittance-meters has a spatial resolution of 0.5 mm and can resolve 1.25 mrad. This choice was made to have a comparable number of non-zero data in space and angle taking into account the beam characteristics at the emittance-meter slits and the 10 % discard of the data due to emittance calculation threshold.

The emittance data were officially analyzed by a Pantechnik developed program but the raw data were also independently analyzed by us. We had the possibility to check the halo, which was not considered as parameter to be checked.

The tests

During the tests, as shown in Fig. 4.5,

Ar^{9+}

Il primo fascio testato sulla SUPERNANOGAN è stato l'Ar9+ il giorno 5/9. La corrente richiesta era pari a 100 A con un'emittanza rms normalizzata per il 90E' stato necessario un lungo condizionamento per ottenere un fascio adeguato ad iniziare il test di stabilità: la figura 2 ne mostra il grafico; la corrente di riferimento era pari a 101 A. Durante la misura la corrente è andata oltre il ś5Nella tabella 4 sono riportati i risultati delle due misure di emittanza effettuate prima e dopo il tests di stabilità: si nota che per entrambe i valori sono entro i limiti richiesti. From Tab. **??** and from Fig. 4.5(a) and 4.5(a) it can be seen that the beam had different characteristics before and after the 2 hours test. First of all the center of the beam changed of about 2 mm (this could be explained taking into account a drift of the magnetic filed of the dipole)mmQuesto può essere

spiegato da un diverso valore di campo magnetico del dipolo (il sistema di controllo gestisce solo la corrente dell'alimentatore, il campo magnetico non è in alcun modo misurato) e da una diversa condizione del plasma che ha portato ad un aumento di emittanza del 20%, comunque entro specifiche.

Table 4.6: $^{36}Ar^{9+}$ emittance measurements results.

	I (μA)	$\epsilon_{rms,\ 100\%}$	$\epsilon_{rms,\ 90\%}$	$\epsilon_{rms,\ 90\%,\ norm.}$	α_x	β_x	$< x >$	$< x' >$
start	105	87	48	0.163	-0.319	0.477	-0.324	4.88
end	102	97	59	0.200	0.070	0.434	1.721	7.73

O^{6+}

Table 4.5 summarizes the source settings of the test on 07/09/2007, the LNL request was 200 μA with a rms normalized emittance of 0.3 mm mrad. In Fig. 4.3(b) the two-hours stability test is shown: the reference current was 205 μA and the *pm*5% limit was exceeded only for 75 s (1.04%).

Table 4.7 shows the results of the two emittance measurements

Table 4.7: $^{16}O^{6+}$ emittance measurements results.

	I (μA)	$\epsilon_{rms,\ 100\%}$	$\epsilon_{rms,\ 90\%}$	$\epsilon_{rms,\ 90\%,\ norm.}$	α_x	β_x	$< x >$	$< x' >$
start	195	87	65	0.285	-0.394	0.488	0.939	5.11
end	211	87	52	0.228	-0.233	0.354	0.859	6.04

Ta^{24+}

The test with the sputtering probe were made just after the O^{6+} test. The requested current was 1μA and no emittance measurement was required.
Table 4.5 shows the source settings and in Fig. 4.3(c) the stability plot is reported. The performed current was 1.45 μA and the ±5% limit was exceeded for 26 s.

Ag^{21+}, Au^{26+} and Au^{30+}

Bibliography

[1] T. A. Antaya and S. Gammino, *The superconducting electron cyclotron resonance 6.4 ghz high-b bode and frequency scaling in electron cyclotron resonance ion source*, Review of Scientific Instruments **65** (1994), no. 1723.

[2] U. Amaldi ed., *Il Centro Nazionale di Adroterapia Oncologica a Mirasole*, Tech. report, INFN-LNF, Frascati, Italy, 1997, The Red Book.

[3] M. Cavenago et al., *Refractory RF oven and sputter probes for electon cyclotron resonance ion sources*, Review of Scientific Instruments **79** (2008), no. 02A301.

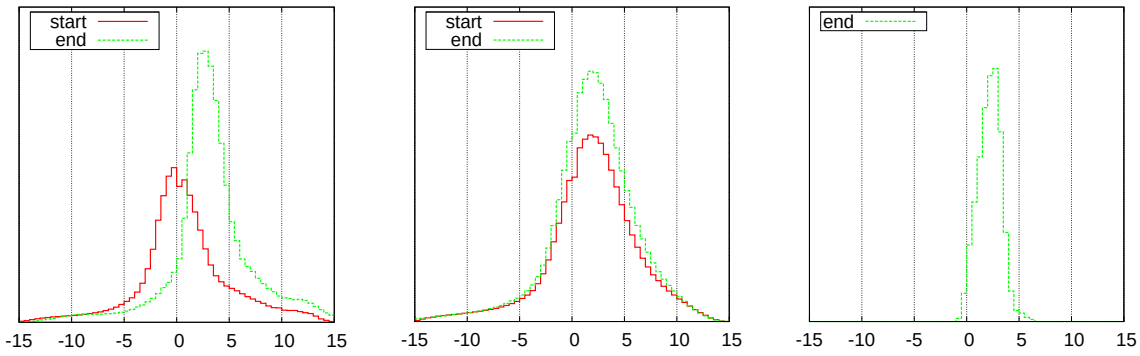

(a) Ar (b) O (c) Au

Figure 4.2: Beam profiles at Faraday cup. The x-axis extremes represent the Faraday cup width.

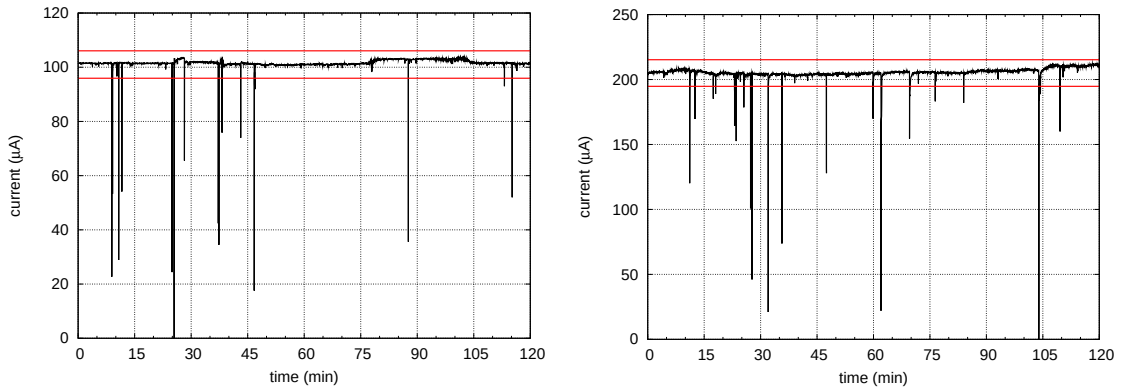

(a) Ar^{9+} (b) O^{6+}

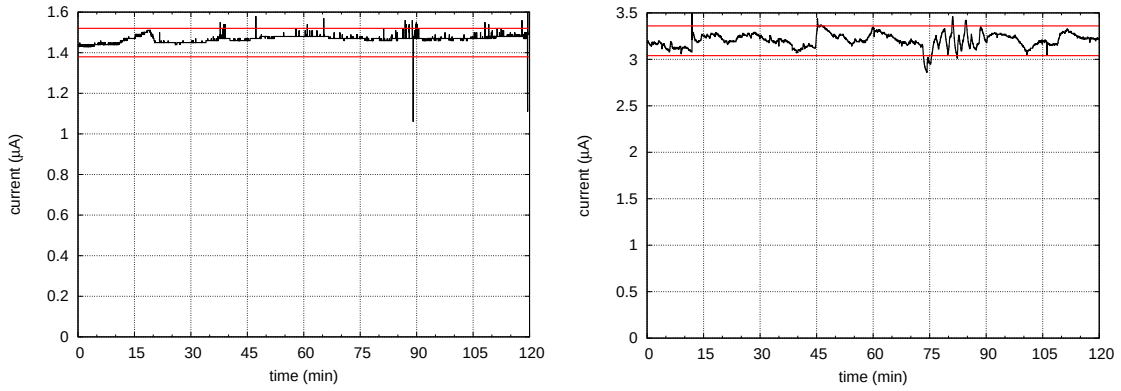

(c) Ta^{24+} (d) Ag^{21+}

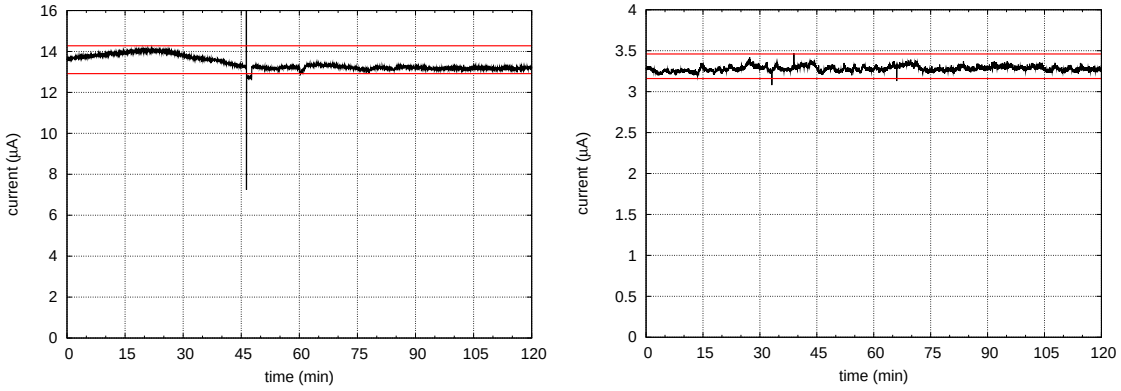

(e) Au^{26+} (f) Au^{30+}

Figure 4.3: 2 hours current stability tests.

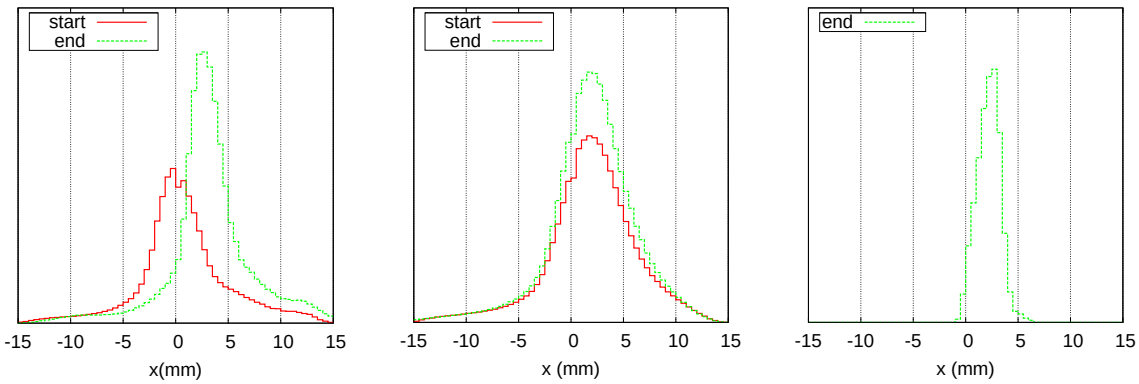

(a) Ar (b) O (c) Au

Figure 4.4: Beam profiles at Faraday cup. The horizontal axis extremes represent the Faraday cup width.

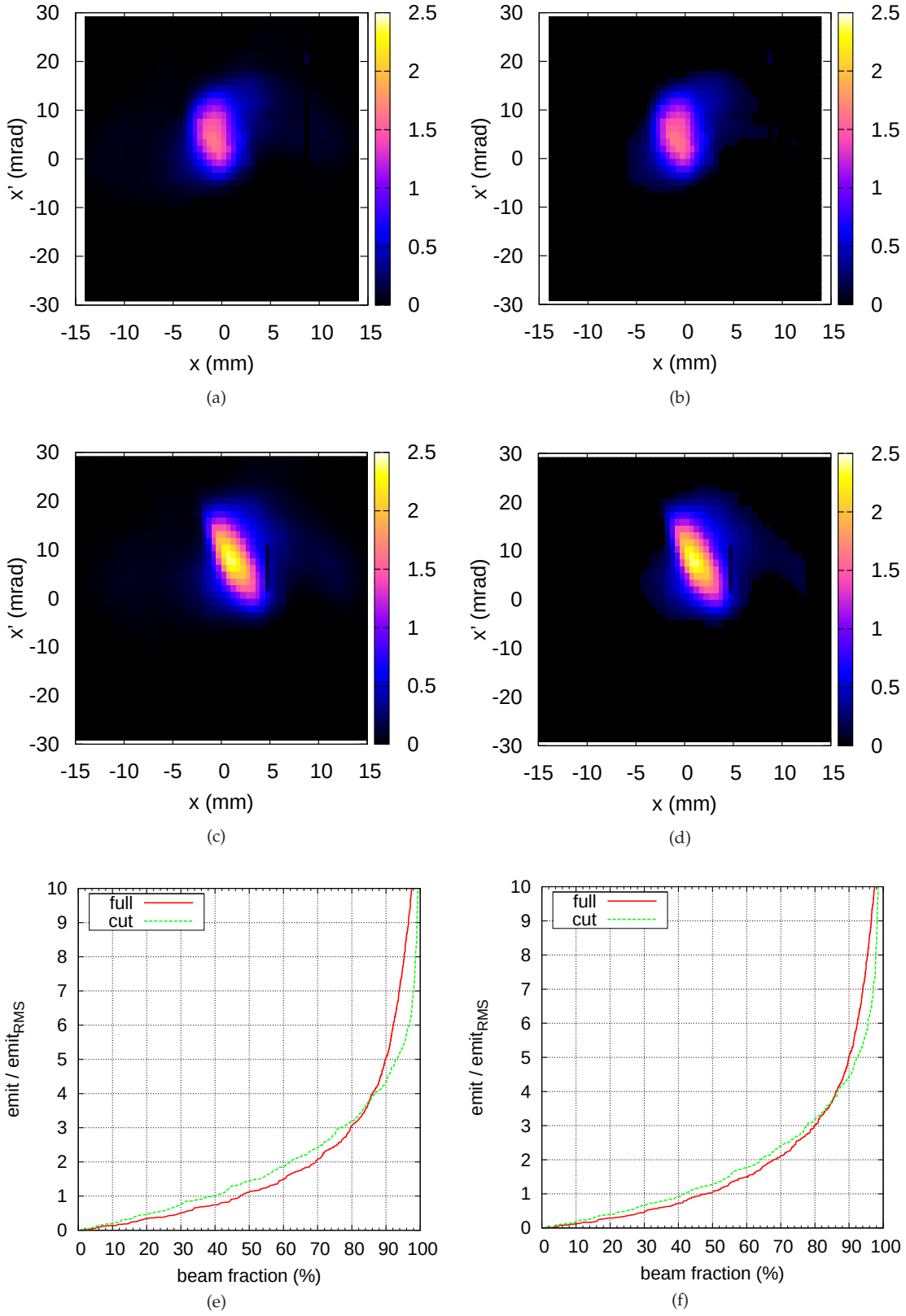

Figure 4.5: Ar graphical summary.

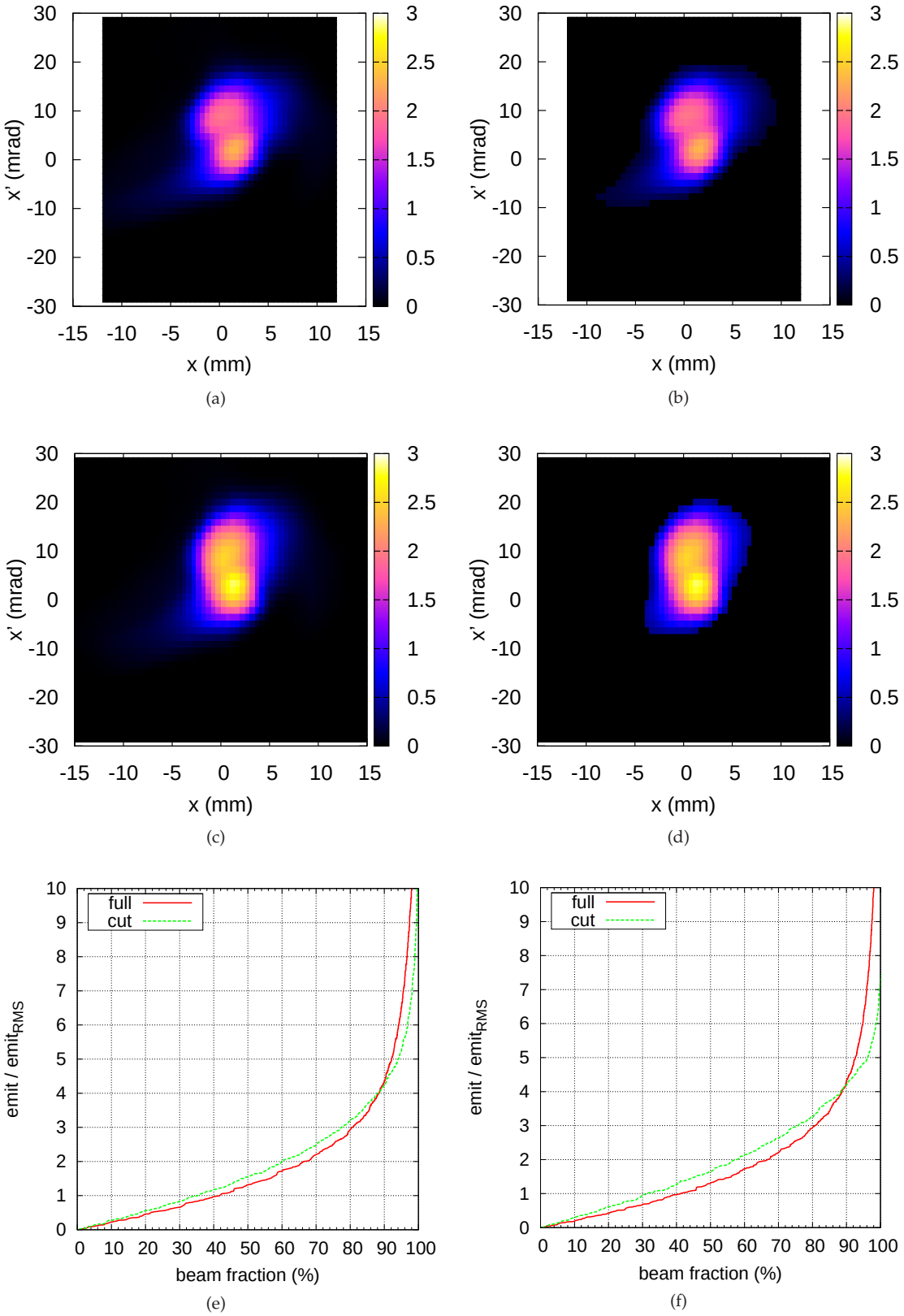

Figure 4.6: O graphical summary.

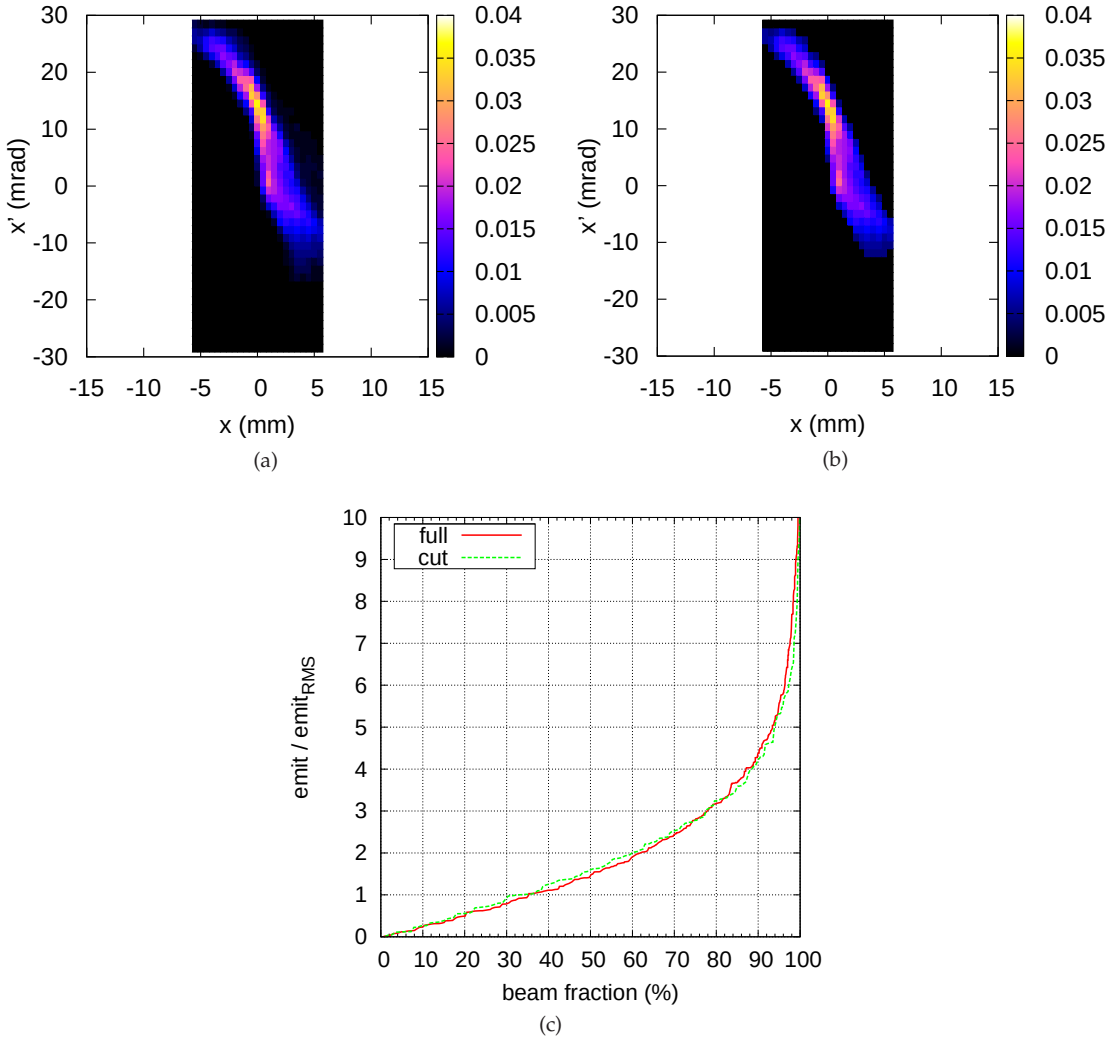

(a) (b) (c)

Figure 4.7: Au graphical summary.

Stripping 5

The least complex and cheapest way to reach higher energies with ALPI is using a stripper station in the middle of the acceleration. This solution allows to enhance the charge state of the ions and therefore it reduces the A/q ratio, which means a greater energy gain per cavity and a lowered magnetic field for quadrupoles and dipoles. Depending on the A/q of the accelerated ion and whether TANDEM or PIAVE is used as injector, at the moment the energy of the beam at the stripper station could vary between 2 MeV/A and 4 MeV/A and it is limited by the present poor performances of the low beta section of ALPI.

During 2007 a study of the stripper solution was performed in order to ensure that the requests of the Agata users group could be satisfied in the future following the funded ALPI upgrade program. The study had the aim to validate the semi-empirical formulas of the literature in this range of energies as well as to predict the behavior of different stripper foil thicknesses on the beam in terms of average charge state and emittance. If the first part of the program was easy to show, the second one was limited by the experimental procedure.

5.1 The physics behind the stripping process

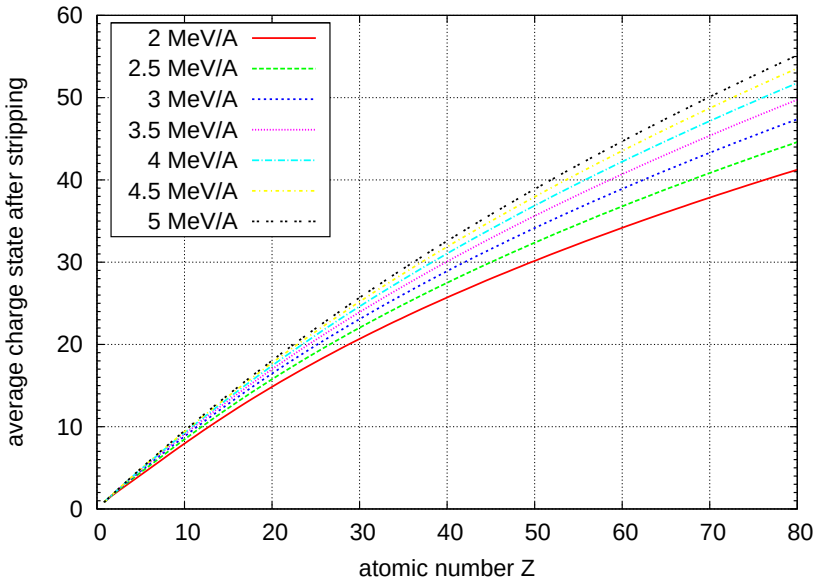

Figure 5.1: Average charge after stripping as function of the atomic number Z and the beam energy in case of equilibrium thickness.

5.2 The experimental work

The experimental set up

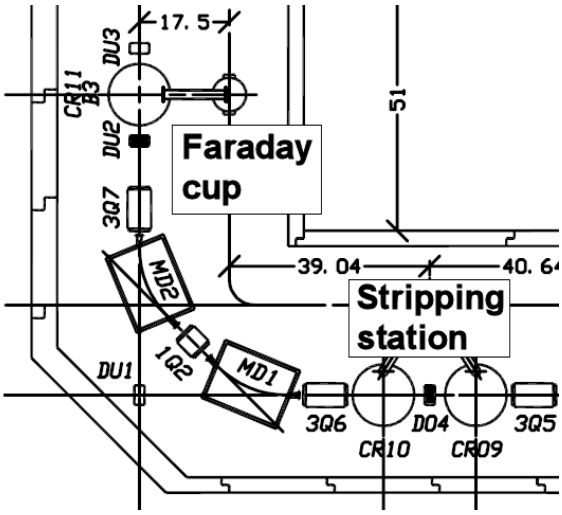

Figure 5.2: Average charge after stripping as function of the atomic number Z and the beam energy in case of equilibrium thickness.

The stripper station was placed in January 2007 in the diagnostic box D04. It foresees a carousel with a hundred of stripper foil holders preceded by a collimator which ensures a proper beam focussing at the foil plane. The system is remote controlled via PC and the carousel is equipped with carbon stripper foils of different thickness, 5-10-20-50 $\mu g/cm^2$. After the stripper station the beam is focalized by 3Q6 triplet and bent by MD1 and MD2, whose magnetic field is measured by a Tesla-meter with a precision of $1/10^6$. The beam passes through 3Q7 triplet (set to off) and then monitored in position (profile grids) and current (Faraday cup) in DU2. The overall scheme is proposed in figure 5.2.

The procedure foresees to record dipole field and current of the collimated beam and then to record field and current of the beam once it has been stripped for the different charge states selected by the dipoles and for different foil thickness.

Experimental results

The average charge for a given ion at a given energy out of a carbon stripper of adequate thickness has been deeply studied during the 60's and 70's by many physicists. Only two semi-empirical formulas derived from the data taken during the two decades for equilibrium thickness foils fit the range between 2 MeV/A and 4 MeV/A, Dmitriev and Nikolaev [ ] and Baron and Delaunay [ ] formula. Betz in [ ] gives a complete review of the previous works but he proposes a formula less accurate than the previous two. Applying the two formulas for various ion and energies it is possible to get the plot in figure 5.1. The experiments have been carried out with 4 different ions: ^{136}Xe, ^{90}Zr, ^{36}Ar and ^{48}Ca. The data plotted in figure **??** show a logarithmic dependence of the average charge on the foil thickness and the slope of the interpolating curves evidences that the equilibrium thickness is achieved with 50 $\mu g/cm^2$ for all beams except ^{136}Xe, which is the heaviest and slowest beam taken into consideration. In table **??** the maximum average charges obtained experimentally are compared with the ones coming from the formulas: only ^{136}Xe is far from the predictions, that means again that the equilibrium thickness in this case has not been achieved.

The data were fitted using the following formula, proposed by and used in:

$$\bar{q}(x) = q_0 + (q_{eq} - q_0)\, e^{-k \cdot x} \tag{5.1}$$

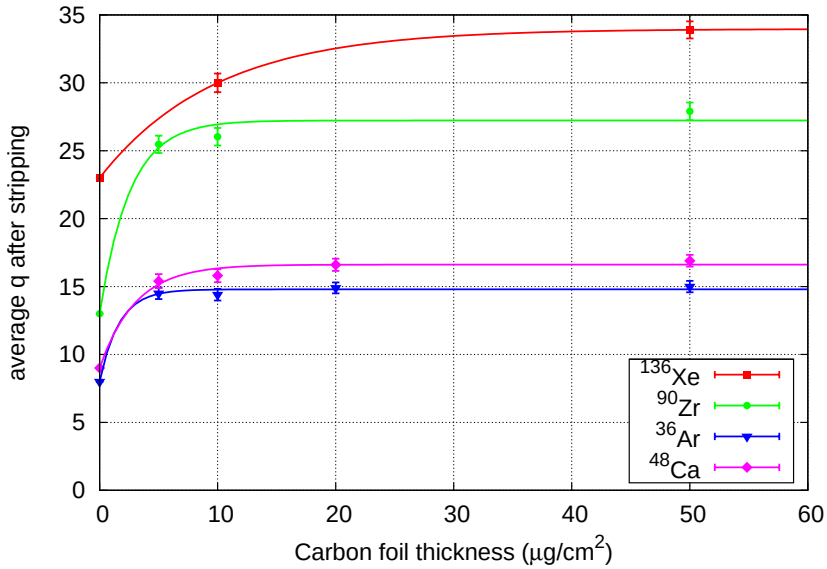

Figure 5.3: Average charge after stripping as function of the target thickness. The continuous line are the weighted exponential fit of the experimental data described in the text (Eq. 5.1).

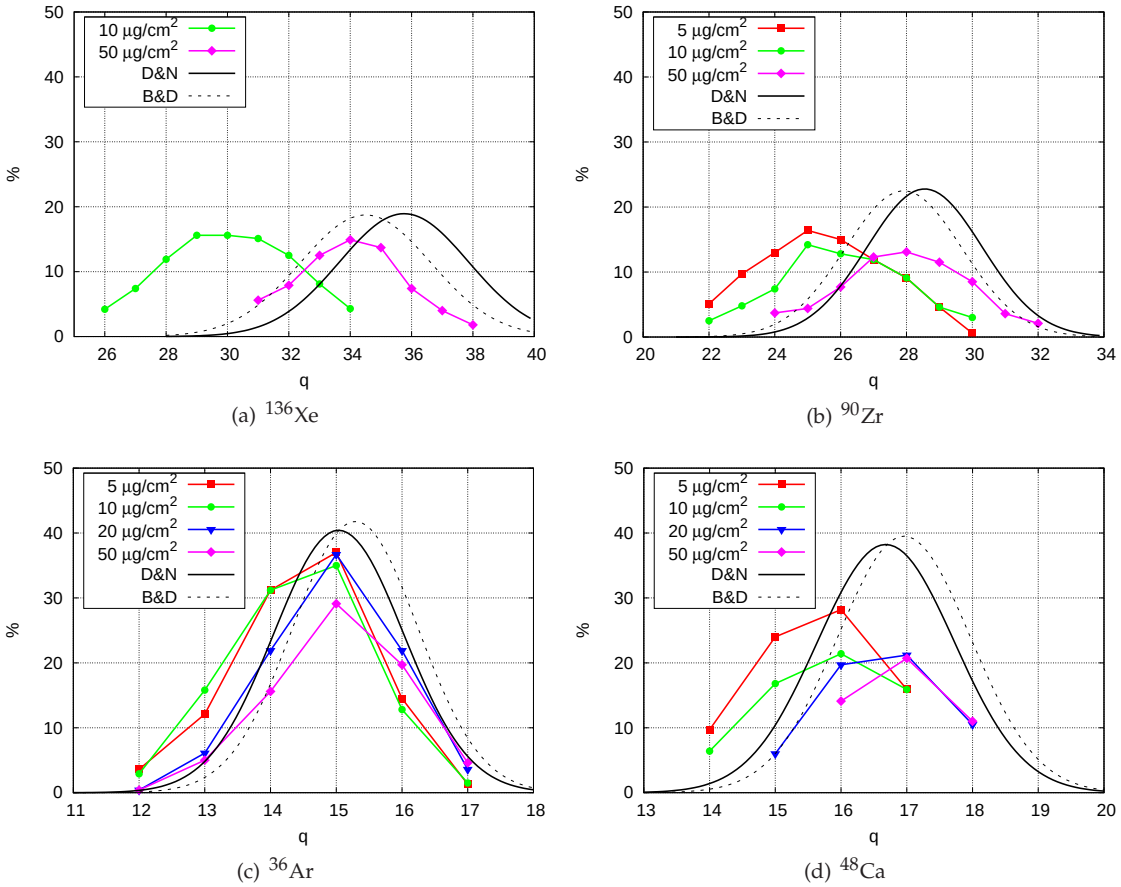

Figure 5.4: Stripping probability curves as function of target thickness. D&N and B&D semiempirical formulas predictions are added as comparison.

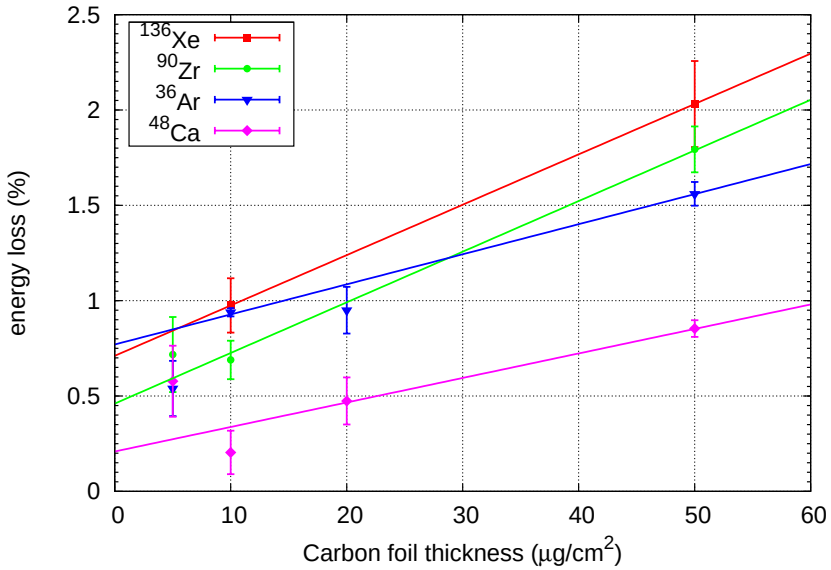

Figure 5.5: Beam energy loss as function of the target thickness. The strait lines are the linear weighted linear fit of the experimental data.

In figure 5.4 the 4 plots of the experimental results are shown. The two smooth curves come from the semi-empirical formulas and show that even if the average theoretical charge is reached there is a problem with the total current of the beam: it decreases while the foil thickness increases. A possible explanation of this result is that the increase of the thickness has a strong influence in beam emittance and part of the beam is thus lost along the line.

5.3 Two examples of accelerated beams after stripping:

Bibliography

[1] J. F. Ziegler, J. P. Biersack, and U. Littmark, *The Stopping and Range of Ions in Solids*, Stopping and Ranges of Ions in Matter, vol. 1, Pergamon Press, New York, 1984.

Table 5.1: Average charge after stripping. The experimental results, both maximum value and the the value coming from the data fit and the semi-empirical predictions are presented.

ion	Z	E (MeV/A)	exp. $\bar{q}$ max	exp. $\bar{q}$ by fit	th. $\bar{q}$ D&N	th. $\bar{q}$ B&D
$^{136}Xe^{23+}$	54	2.475	33.9 ± 0.4	33.9	35.8	34.5
$^{90}Zr^{13+}$	40	2.614	27.9 ± 0.7	27.2 ± 0.7	28.5	27.9
$^{36}Ar^{8+}$	18	3.206	15.0 ± 0.4	14.8 ± 0.1	15.0	15.3
$^{48}Ca^{9+}$	20	3.487	16.9 ± 0.3	16.6 ± 0.2	16.7	17.0

Table 5.2: Beam energy loss as function of target thickness. The data come from the fit shown in Fig. 5.2 and they are compared to the data calculated by Ziegler's SRIM program [1].

ion	Z	E (MeV/A)	stopping power (keV/μg/cm^2)		error on E
			by fit	by SRIM	(%)
$^{136}Xe^{23+}$	54	2.475	89 ± 22	82.9	0.71 ± 0.16
$^{90}Zr^{13+}$	40	2.614	62 ± 6	58.1	0.46 ± 0.08
$^{36}Ar^{8+}$	18	3.206	18 ± 3	19.4	0.77 ± 0.05
$^{48}Ca^{9+}$	20	3.487	22 ± 6	22.7	0.21 ± 0.15

The upgrade scenarios 6

Three upgrade scenarios for PIAVE-ALPI complex are foreseen, with an increase of final energy and beam quality as a result. The upgrades are organized in stages following a costs optimization criterion, which means that the specifications for new equipments are given keeping in mind the final stage and the intermediate solutions do not waste previous capital investments.

The are three suggested scenarios. The first one is called "AGATA" and its specifications derive from the present limits of PIAVE-ALPI accelerator complex. The aim is to fulfill the AGATA user groups requests without changing the upgrade plans for the near future which are already decided. The last scenario is called "SPES" and it implies a radical change in PIAVE layout and in the overall ALPI performances. It needs a full funding support and it represents the maximum utilization of ALPI accelerating structures. The intermediate scenario,"intermezzo", gives the chance to get a substantial improvement of "AGATA" scenario with little effort.

6.1 Preliminary considerations

The performances of the medium beta cavities installed in ALPI have improved year by year. The last release of the inner structure (beam ports and stem) and accurate polishing techniques allow to use them safely at 4.5 MV/m [1]. Therefore an average E_{acc} of 4.2 MV/m is foreseen for next year and once all the cavities are replaced it is possible to reach an average E_{acc} of 4.5 MV/m.

As we have said before, the situation of the low beta cavities is more delicate. In order to make them work at fields higher than 3.5 MV/m a cooling system for the RF coupler and a resigned are required [2]. The CRO3 cryostat is ready to use the new solution and the expected average E_{acc} is 5 MV/m. More years are needed to complete the low beta cryostats upgrade, but an average E_{acc} is 6 MV/m is foreseen in the future.

6.2 AGATA

6.3 Intermezzo

6.4 SPES

As we have said before the weakness of Piave layout (see Fig. 6.4(a)) at 5 MV/m is the absence of a proper bunching section before the QWR cryostats since the first cavity is used as buncher. Moreover the use of alternating synchronous phases with a doublet focusing system produces different envelopes for x and y plane causing different emittance increase, as reported in the second column of Tab. 6.2. The compactness of the layout, which in principle could have many advantages in shortening the transverse and longitudinal period, is a problem if it compromises the diagnostics placing as it happens in Piave, where the first diagnostic box downstream the SRFQ is placed after the two QWR cryostats. To do a proper and more comfortable set-up of the

Table 6.1: ALPI QWR estimated performances for the upgrade scenarios.

cryostat	AGATA	intermezzo	SPES
low beta (β = 0.047 and β = 0.056)			
CR01-02	n/a	n/a	6
CR03	5	6	6
CR04-06	3.5	6	6
medium beta (β = 0.11)			
CR07-18	4.2	4.5	4.5
high beta (β = 0.13)			
CR19-20	5.5	5.5	5.5
CR21	n/a	n/a	5.5

injector a diagnostic box would be very useful just after the SRFQ to check the input match in current and between the two cryostats to check if any loss occurs due to misalignment of beam, cavity or doublet.

6.4.1 The new Piave layout

For this reason a new layout (see Fig. 6.4(b)) is proposed.

Bunching section. A new low energy buncher is foreseen. The buncher is relaized by modification of HEB2 keeping the QWR resonant cavity and all the ancillaries (RF amplifier, electronics, cooling system, support) and changing the internal stem and gaps width. To take full advantage of the new buncher a thin (L_{eff}=15.6 cm) low gradient (<20 T/m) quadrupole is placed between the SRFQ and the buncher in the x-plane waist in order to reverse the transverse beam divergence without affecting the quadrupole symmetry. After the buncher the 2PQ5 doublet focuses the beam at the first QWR cavity and the round condition could be achieved setting appropriately the singlet field.

New cryostats. The 80 MHz QWR developed in Legnaro are able to sustain 6 MV/m at 7 W in good helium pressure regime. The old Piave layout wastes the opportunity of high gradient beam dynamics because of the funnel-shaped use of the synchronous phases, where the E_{acc} must be lowered to obtain a wider longitudinal acceptance. The solution found at ISAC2 (TRIUMF) for heavy ion acceleration fulfills our requirements as well. The cryostat was design to house four 106 MHz QWR cavities and a compact super-conducting solenoid (max 9 T) as ahown in Fig. 6.5. The big advantage of this solution is to change the longitudinal periodical conditions of the beam since the distance between the two cavities facing the solenoid is very close to the one between the two cavities facing the space between cryostats. This means having a longitudinal period which is double the transverse period and the full gradient acceleration could be accepted. From the point of view of transverse focusing, the solenoids give the unique opportunity of maintaining equal conditions for x and y plane and having a round beam along the acceleration as a result. Morover, between the cryostats in addition to the space for the vacuum valves a diagnostic box and a steerer is foreseen. This allows to check the transverse conditions between the two cryostats in the focal point of the solenoid as it happens in the ALPI period. This diagnostics combined to one placed after 2PQ5 will be used to check the correct transverse match parameters and in particular the roundness of the beam before entering the first cryostat.

New HEB1 location. Since the new QWR cryostats are longer and the bunching section has been added, the HEB1 buncher cannot be in the same position as before because is too close to

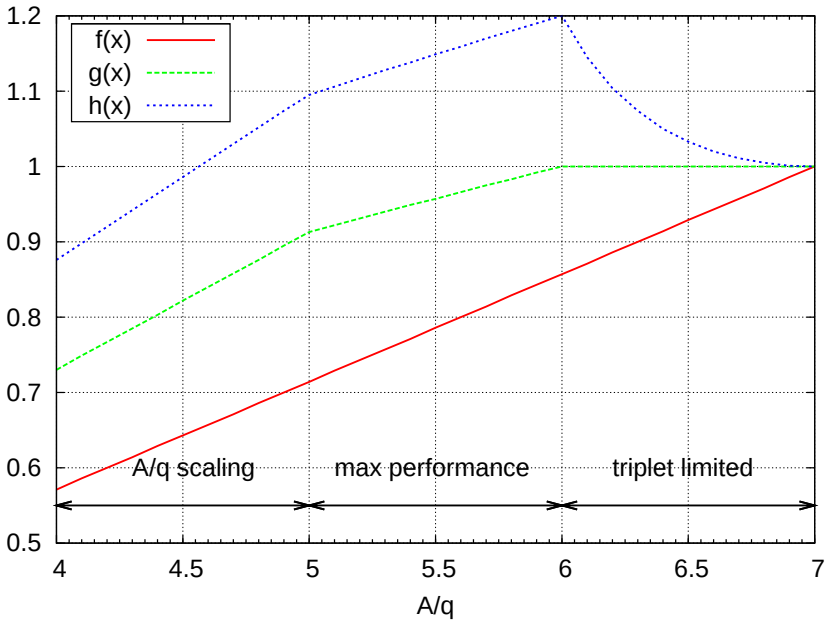

Figure 6.1: ALPI low energy branch QWR accelerating field modulation factors in the "AGATA" scenario.

Table 6.2: Old and new layout beam dynamics results comparison.

	SRFQ out	old PIAVE	new PIAVE	unit	*var.*
$\varepsilon_{x\ rms}$	0.100	0.102	0.105		*+3%*
$\varepsilon_{y\ rms}$	0.100	0.138	0.105	mm mrad norm.	*-24%*
$\varepsilon_{z\ rms}$	0.060	0.163	0.066		*-60%*
E	0.59	1.24	1.45	MeV/A	*+17%*

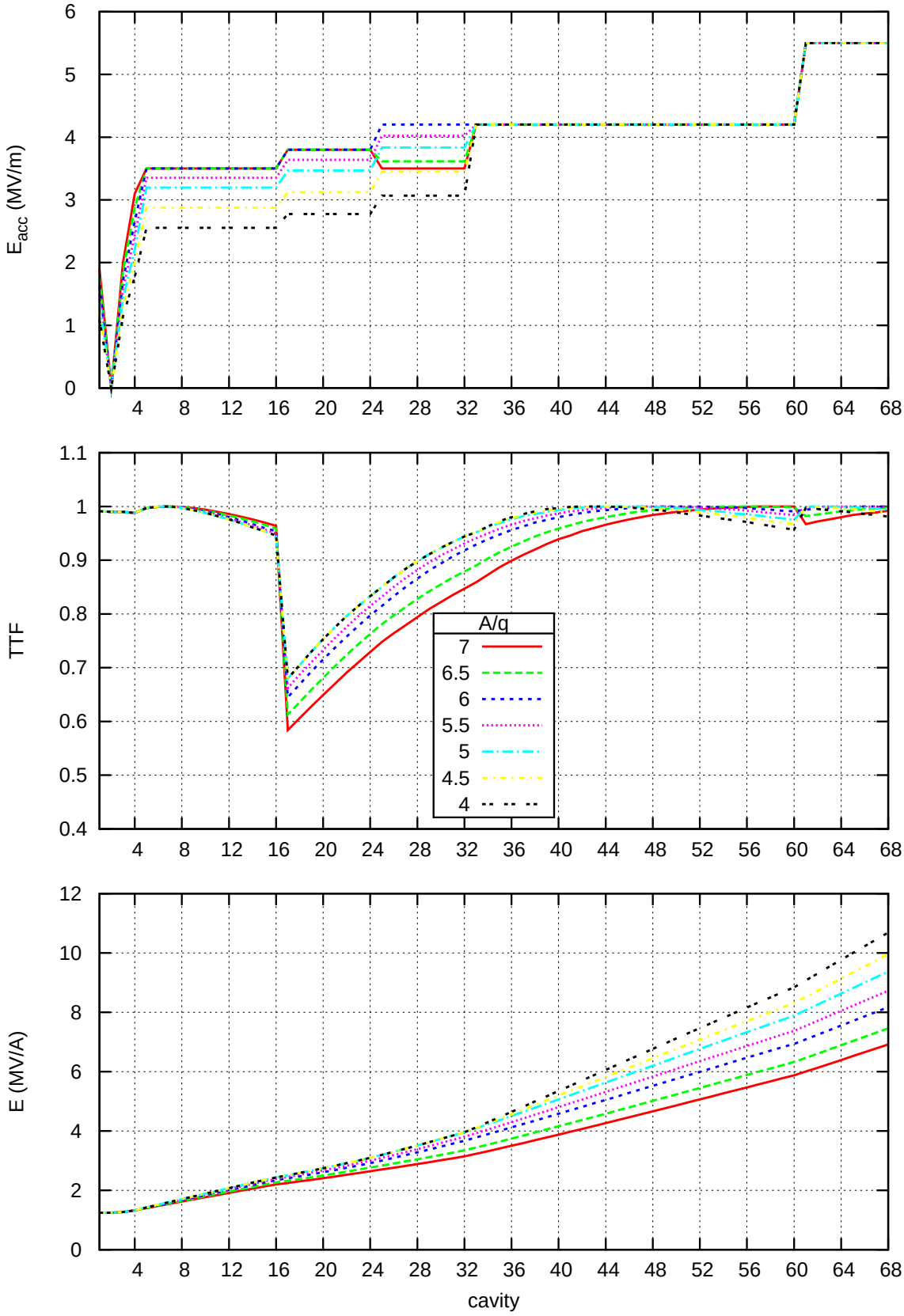

Figure 6.2: Performances of ALPI for scenario "AGATA".

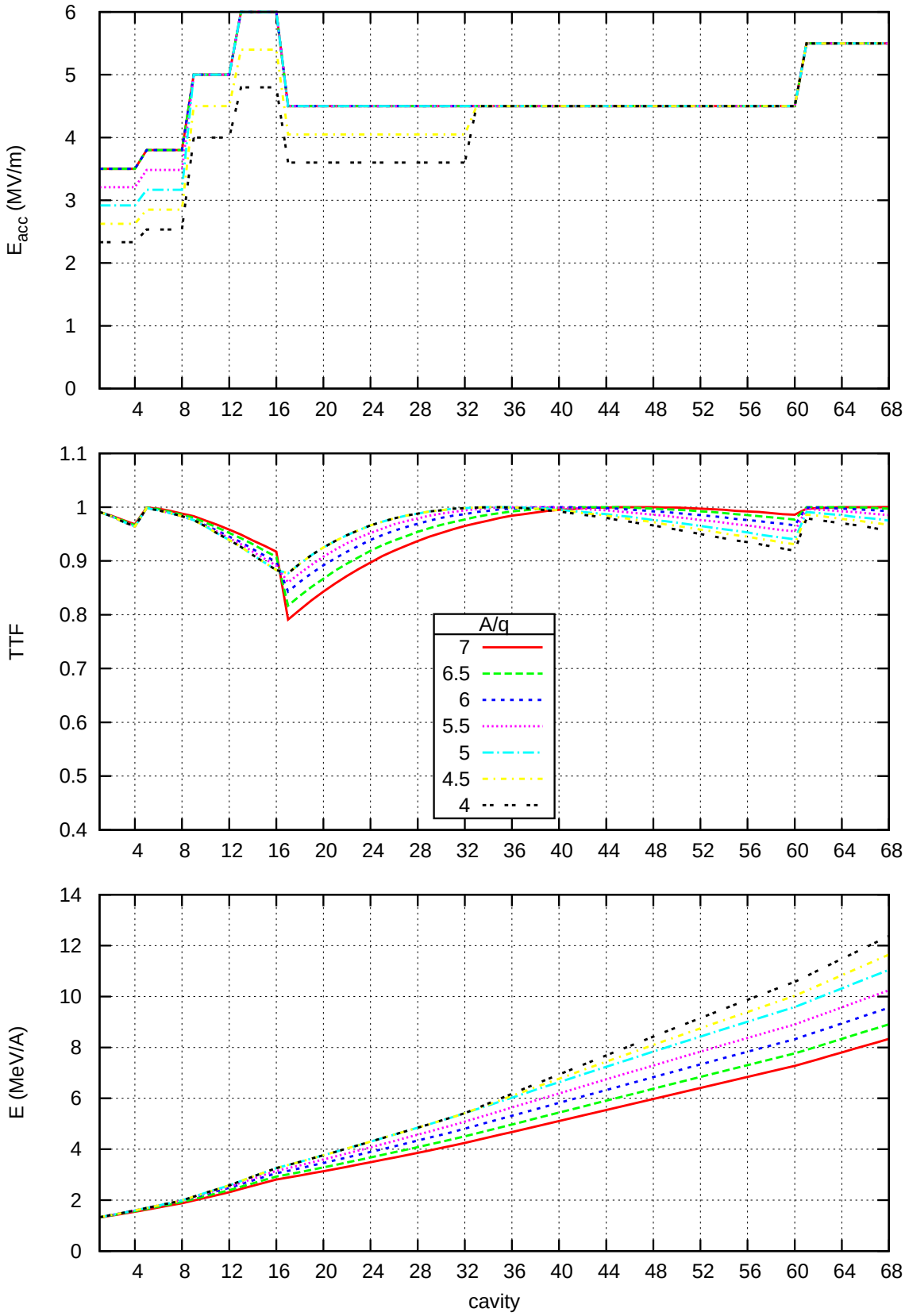

Figure 6.3: Performances of ALPI for scenario "intermezzo".

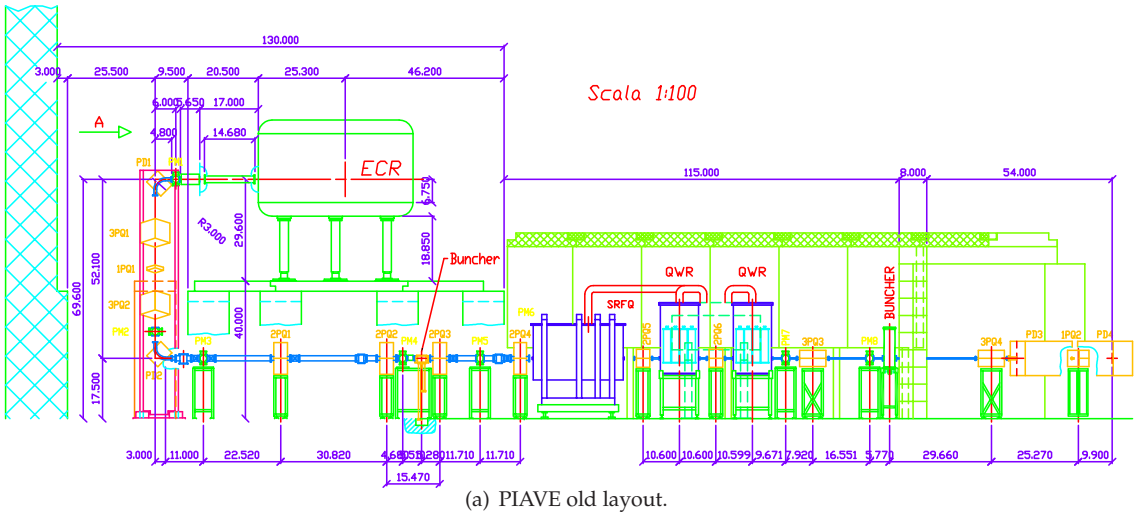

(a) PIAVE old layout.

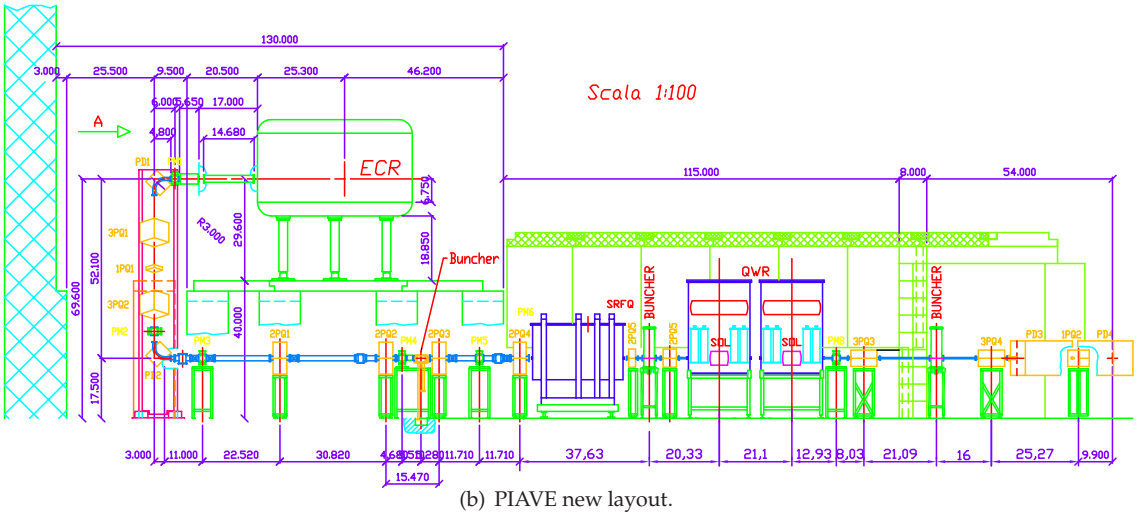

(b) PIAVE new layout.

Figure 6.4: PIAVE layout comparison.

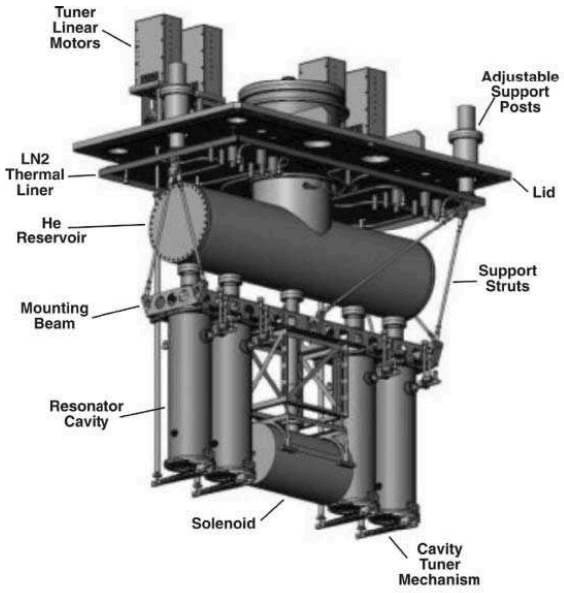

Figure 6.5: ISAC2 cryostat 3D view.

the last super-conducting cavity. Therefore the HEB1 will be moved after the shielding wall in the room common to the injecting and extracting lines of ALPI and a proper shielding will be tailored around it.

In Table 6.2 the beam dynamics results of new layout are compared to the ones of the old layout. With the new layout we can reach a very low longitudinal emittance growth (10%) doubling the energy of the beam and the transverse emittance increase is limited to 5% and it is equal in the x and y plane.

The further advantage of this solution is to operate the injector even with a single cavity failure, which was not possible to perform in the old layout. Table 6.3 shows the results of a set of simulations which are performed optimizing output Twiss parameters, which means round beam and longitudinal parameters compatible to the parallel transport in the L-bend section. The results are quite encouraging because the output energy is all cases is higher than the reference output energy in the old layout and the emittance growth is of the same order of magnitude of the new reference design. The asymmetry of the transverse emittance increase in most of the cases comes from a different focusing at the buncher location to ensure the symmetric envelope along the acceleration.

Table 6.3: New Piave beam dynamics results in case of a single cavity failure.

	all	1.1 off	1.2 off	1.3 off	1.4 off	2.1 off	2.2 off	2.3 off	2.4 off	unit
$\varepsilon_{x\ rms}$	*0.105*	0.105	0.105	0.100	0.104	0.101	0.100	0.103	0.103	
$\varepsilon_{y\ rms}$	*0.105*	0.108	0.105	0.102	0.103	0.103	0.102	0.104	0.105	mm mrad n.
$\varepsilon_{z\ rms}$	*0.066*	0.065	0.070	0.062	0.063	0.063	0.063	0.064	0.065	
E	*1.45*	1.37	1.31	1.35	1.36	1.34	1.34	1.33	1.31	MeV/A

6.4.2 ALPI upgrade

As a consequence of the new Piave layout two low beta "traditional" cryostats become available. This means that the ALPI low beta part could be extended at the minor cost of 8 new QWR cavities and ancillaries (RF amplifiers, control electronics,vacuum system) and the link to the present cryogenic system which is planned to be upgraded (20% more of cryogenic power) in few years.

In order to hold a complete new period few changes have to be made in the structure. A new quadrupole triplet is foreseen just before CRO1 and 3Q2 will be moved half way from 3Q1 and 3Q2-bis. The period between 3Q2 and 3Q2-bis is used to a new 80 MHz buncher which is probably super-conducting since an equivalent voltage of 250 kV is required.

As a consequence

Bibliography

[1] S. Stark, A.M. Porcellato, and al., *Progress in the ALPI-PIAVE low-beta section upgrade*, Proceedings of the 13th International Workshop on RF Superconductivity (Peking, China), 2007.

[2] D. Zenere, A. Facco, and F. Scarpa, *Progress in the ALPI-PIAVE low-beta section upgrade*, Proceedings of EPAC08 (Genoa, Italy), 2008, pp. 3413–3415.

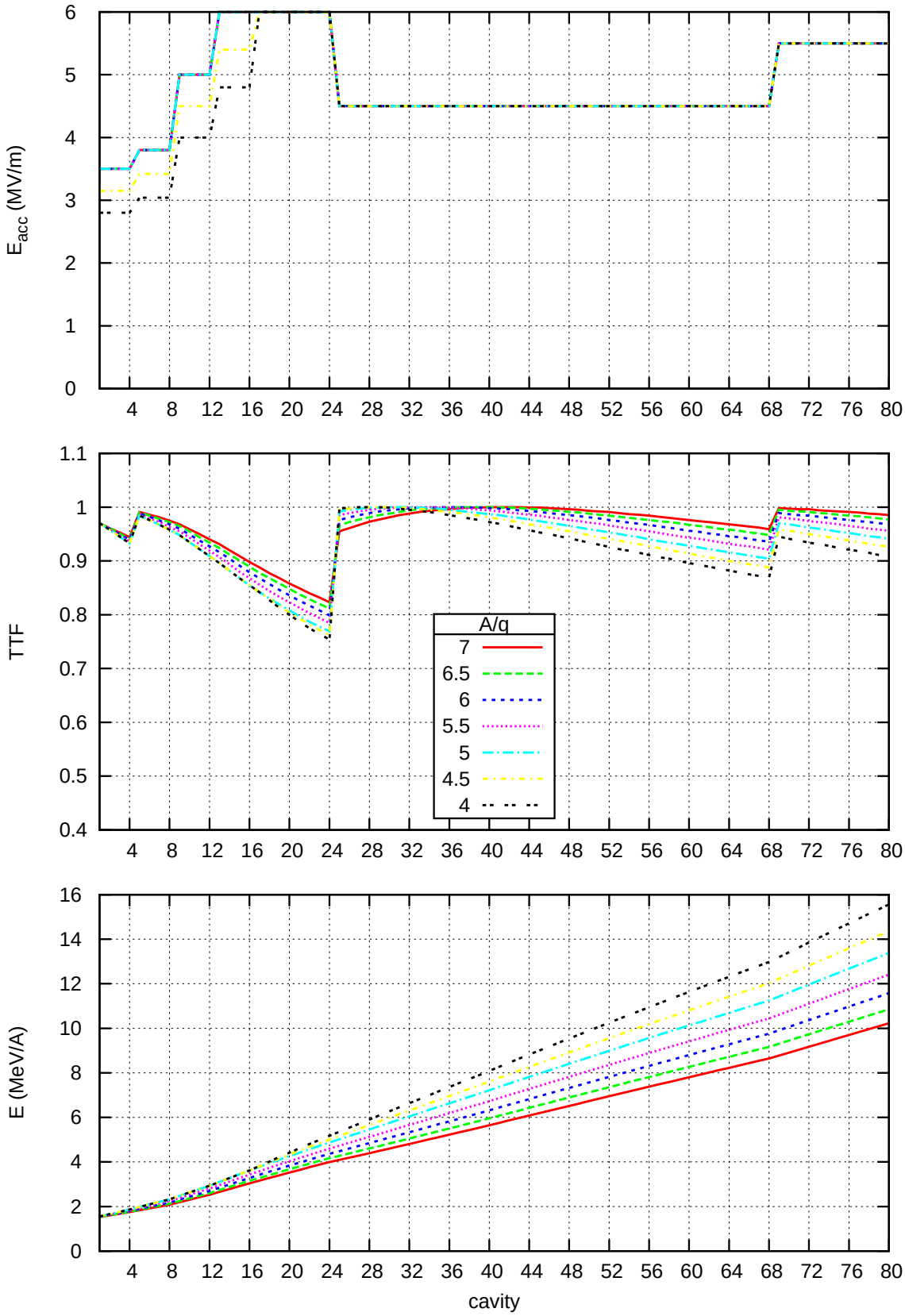

Figure 6.6: Performances of ALPI for scenario "SPES".

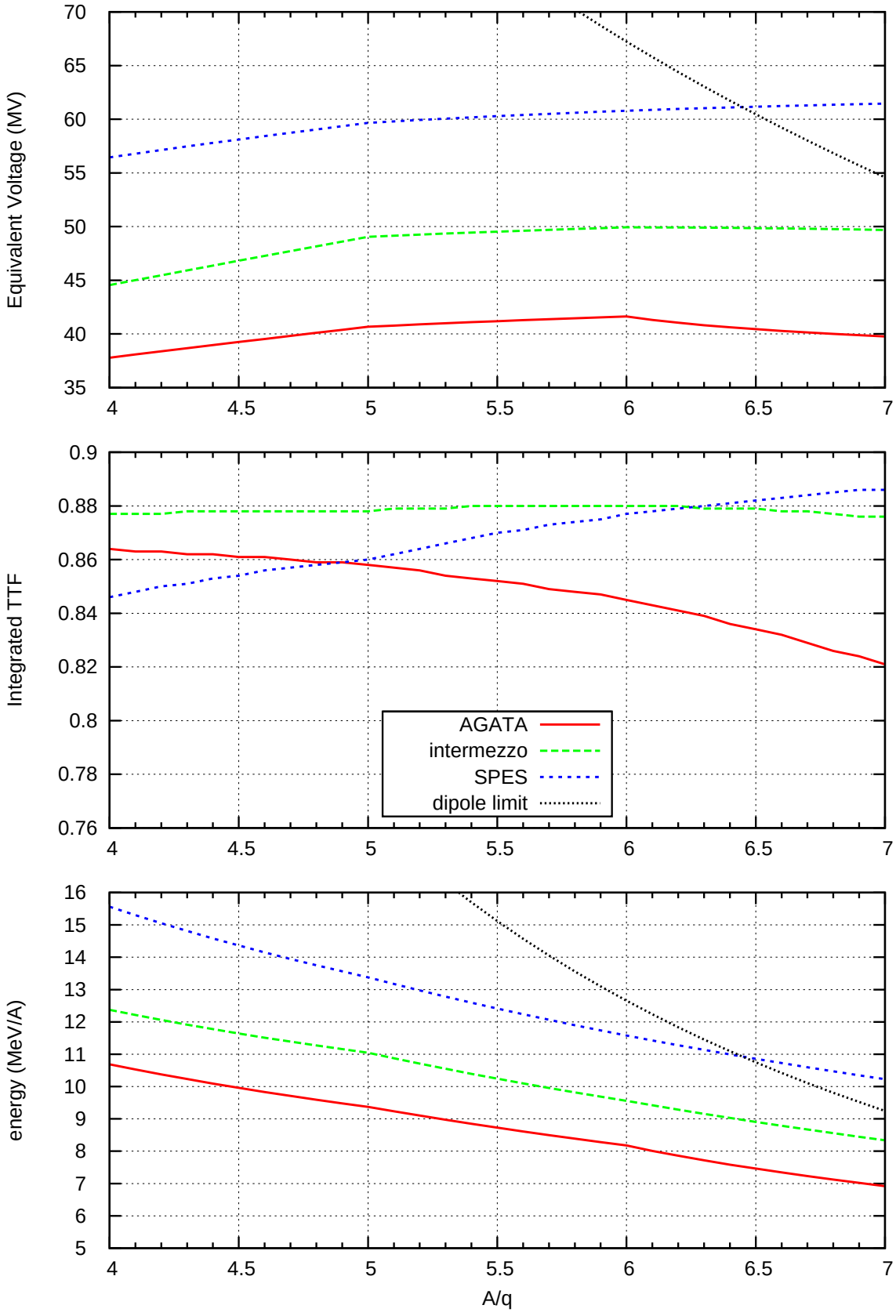

Figure 6.7: ALPI upgrade scenarios performances. The colored lines represent the different upgrade scenarios and the black line the limits given by the maximum field of the dipoles 1.6 T (3.9 Tm).

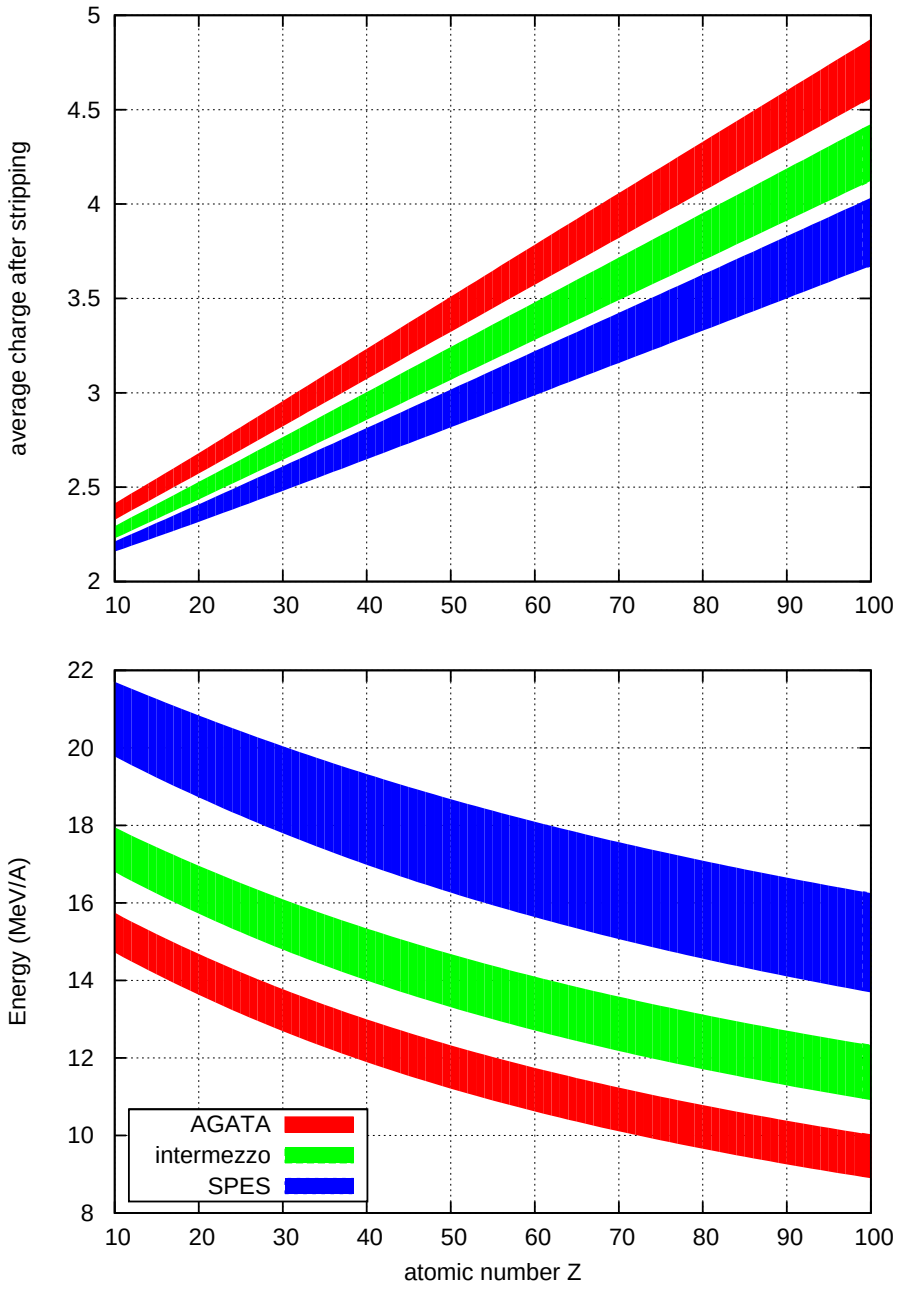

Figure 6.8: ALPI upgrade scenarios performances using strippers.

Useful nuclear derivations

A

A.1 The semi-empirical mass formula

The mass of a nucleus defined by A and Z is given by

$$M(A,Z) = Z\, m_H + (A-Z)\, m_n - B(A,Z)/c^2. \tag{A.1}$$

The semi-empirical mass formula, based on the liquid drop model, considers five contributions to the binding energy:

1. The volume term $a_V\, A$. Since the nuclear force is saturated, each nucleon contributes about 16 MeV to the binding of the nucleus.
2. The surface term, which gives the reduction in binding resulting from the reduced binding at the nuclear surface, $-a_S\, A^{2/3}$.
3. The Coulomb term, which represents the Coulomb repulsion of the $Z\ (Z-1)/2$ pairs of protons in the nucleus. For a spherical nucleus of radius $R = r_0 A^{1/3}$ with the charge spread evenly throughout the sphere the Coulomb energy is

   $$-\frac{3}{5}\frac{1}{4\pi\epsilon_0}\frac{Z(Z-1)e^2}{r_0 A^{1/3}}.$$

   For a general charge distribution not too different from the above, this can be parameterized as $-a_C\, Z^2\, A^{-1/3}$.
4. The asymmetry term, which accounts for the difference between proton and neutron number. If there were no Coulomb interaction between protons, we would expect, from symmetry arguments applied to a Fermi gas, to find equal numbers of protons and neutrons. In order to generate the observed neutron excess (in most nuclei) we need to shift nucleons from the "proton side" to the "neutron side" of these two Fermi gases. These neutrons can only be added above the Fermi level, so energy must be put into the system. This is the asymmetry energy which reduces the nuclear binding. Note that the system is symmetrical about $N = Z$; the same energy would be required to shift nucleons the other way if we require a proton excess. Thus to lowest order, we can expect the energy to vary as $(N-Z)^2$; in addition, the Fermi gas energy level spacing varies as 1/A so that the asymmetry term is

   $$-a_A\frac{(A-2\,Z)^2}{A}.$$

5. An emp=irical term to take into account the observed pairing of nuclei:

   $$\delta(A,Z) = \begin{cases} +\delta_0 & \text{Z and N even (A odd)} \\ 0 & \text{A odd} \\ -\delta_0 & \text{Z and N odd (A odd)} \end{cases}.$$

We note that of 342 (beta-) stable nuclei in the 1993 mass compilation, there are are 209 with even A, even Z; 70 with odd A, even Z; 59 with even A, odd Z and only 4 with odd A and Z (^{2}H, ^{6}Li, ^{10}B, ^{14}N). Clearly pairing enhances stability (or binding energy). This can also be seen, for instance, in the neutron separation energies of neighboring isotopes, etc.

The binding energy is thus

$$B(A,Z) = a_V\, A - a_S\, A^{2/3} - a_A \frac{(A-2\,Z)^2}{A} - a_C\, Z^2\, A^{-1/3} + \delta_0(A,Z). \tag{A.2}$$

The coefficients are determined by fitting to a suitably large data set of masses (hence semi-empirical). A typical set is (all values in MeV):

$$a_V = 15.8, \qquad a_V = 18.3, \qquad a_V = 0.714, \qquad a_V = 23.2, \qquad \delta_0 = \frac{12}{A^{1/2}}. \tag{A.3}$$

A.2 The line of stability

Greater binding energy per nucleon implies greater stability. It is most convenient to explore this in the context of a set of isobars, i.e. a set of nuclides with the same A. These can transform into one another by various forms of beta decay.

The masses of the members of a set of isobars can be obtained by rearranging the semiempirical mass formula A.1:

$$M(A,Z) = \alpha\, A - \delta(A,Z) + \beta\, Z + \gamma\, Z^2,$$

where

$$\begin{aligned} \alpha &= m_n\, c^2 - a_V + a_A + a_S^{-1/3} \\ \beta &= (m_H - m_n)\, c^2 - 4a_A - a_C\, A^{-1/3} \\ \gamma &= a_C\, A^{1/3} + 4a_A/A \end{aligned} \quad .$$

This equation has the form of a parabola for fixed A; we can solve for the value of Z giving the greatest binding energy (smallest mass), i.e. the most stable isobar. Thus

$$\frac{\partial}{\partial Z} M(A,Z) = 0$$

yields

$$Z_S = \frac{-\beta}{2\gamma} = \frac{A/2 + (m_n - m_H)c^2 A/8a_A + a_C A^{2/3}/8a_A}{1 + \frac{1}{4}(a_C/a_A)A^{2/3}}. \tag{A.4}$$

Inserting the values for the coefficients A.3 and rearranging,

$$Z_S = \frac{A\left(1 + 0.0077\, A^{-1/3}\right)}{2 + 0.0154\, A^{2/3}}. \tag{A.5}$$

This then gives the equation for the "valley of stability" on the (N,Z) chart of nuclides. Note that is determined by an interplay between the Coulomb force (makes Z a minimum) and the asymmetry term (makes $N = Z$).

In Fig. A.1 the curve coming from Eq. A.6 is superimposed on the experimental valley of stability. The agreement for the most frequent isotope is very good, with an error of maximum 1 proton (1 neutron).

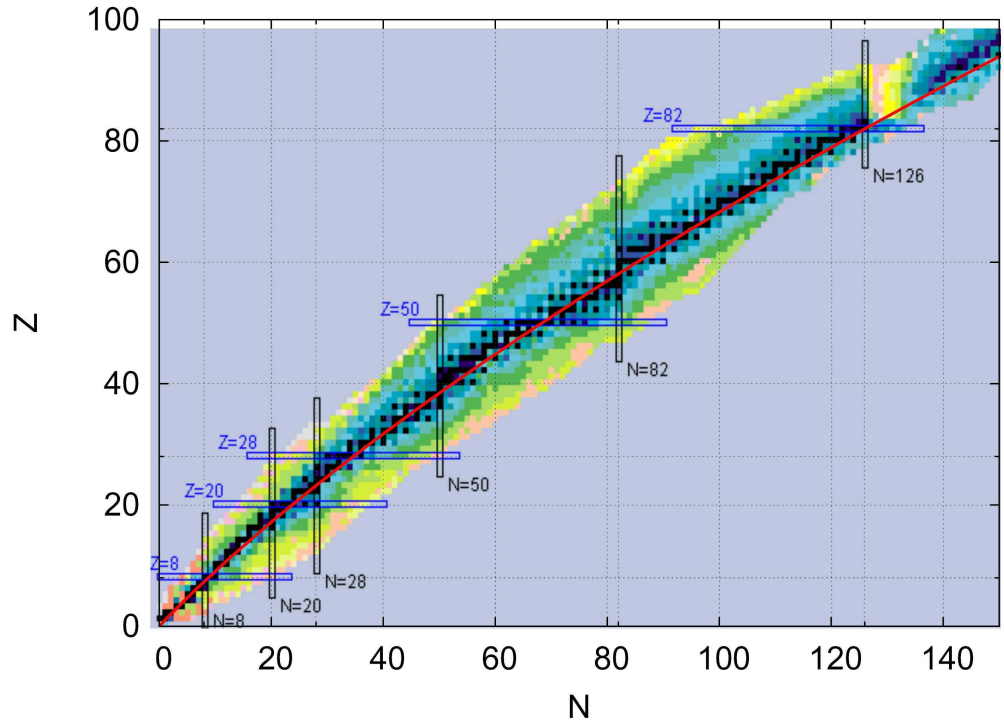

Figure A.1: The valley of stability. The red curve comes from Eq. A.6 and the background image from HTTP://WWW.NNDC.BNL.GOV/NUDAT2/.

A.3 Coulomb barrier

The Coulomb barrier is the energy barrier resulting from electrostatic interaction that two nuclei must overcome in order that they can approach closely enough to undergo nuclear fusion. The Coulomb barrier is produced by electrostatic potential energy. In the fusion of light elements to form heavier ones the positively charged nuclei must be forced close enough together to cause them to fuse into a single heavier nucleus. The force between nuclei is repulsive until a very small distance separates them, and then it rapidly becomes very attractive. Therefore, in order to surmount the Coulomb barrier and bring the nuclei close together where the strong attractive forces operate, the kinetic energy of the particles must be as high as the top of the Coulomb barrier.

The Coulomb electrostatic potential for two colliding nuclei at radius d could be expressed as

$$U(Z_1, Z_2) = \frac{1}{4\pi\epsilon_0}\frac{Z_1 Z_2 e^2}{d}, \tag{A.6}$$

where $\epsilon_0 = 8.85 \times 10^{-12}$ $C^2N^{-1}m^{-2}$ and $e = 1.60 \times 10^{-19}$ C.

The nuclear radius is conventionally set to $r(A) = r_0 A^{1/3}$ with $r_0 = 1.44 \times 10^{-15}$ m. In principle the Coulomb barrier could be overcome if the distance is lower than the sum of the nuclear radii of the two nuclei. Therefore $d = r_0(A_1^{1/3} + A_2^{1/3})$.

Substituting the previous expression in Eq. A.6 it results

$$U(Z_1, Z_2)[\text{MeV} \simeq \frac{Z_1 Z_2}{A_1^{1/3} + A_2^{1/3}}, \tag{A.7}$$

which is the minimum energy to overcome the barrier in the center-of-mass frame. To obtain the

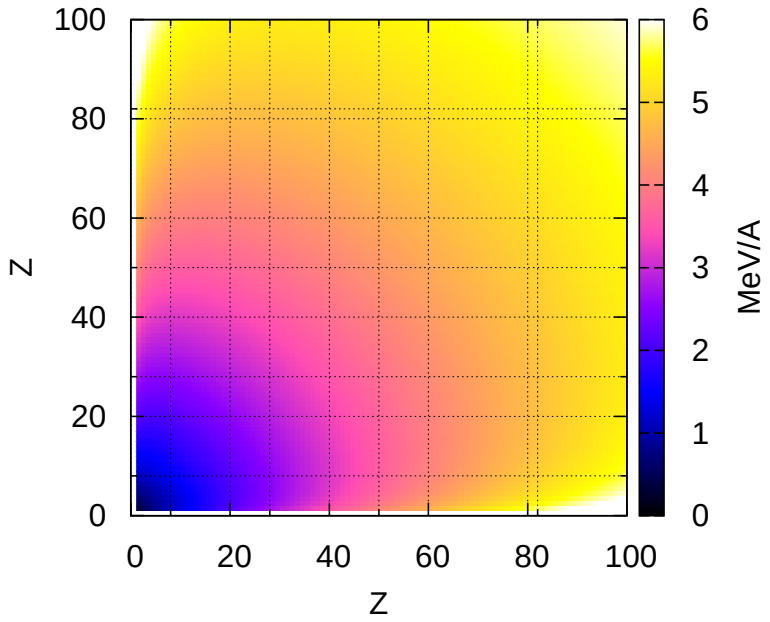

Figure A.2: Coulomb barrier for the most frequent isotopes appearing in the valley of stability.

lab frame expression we must multiply by the factor $(A_1 + A_2)/A_2$ resulting

$$U(Z_1, Z_2)[\text{MeV/A} \simeq \frac{A_1 + A_2}{A_1 A_2} \frac{Z_1 Z_2}{A_1^{1/3} + A_2^{1/3}}. \tag{A.8}$$

Combining the previous expression with Eq. A.6 we can obtain the Coulomb barrier for the most frequent isotopes appearing in the valley of stability, plotted in Fig. A.2.

Various calculations

B

B.1 RMS vs FWHM

The one dimension Gaussian function is defined as

$$f(x) = \frac{1}{\sigma\sqrt{2\pi}} e^{-(x-x_0)^2/2\sigma^2}, \tag{B.1}$$

where σ represents the Root Mean Square value of the distribution. If we want to express σ in terms of Full Width Half Maximum, quantity which is easier to be determined from a graph or from an analogical oscilloscope screen, we solve

$$e^{-(x-x_0)^2/2\sigma^2} = \frac{1}{2} f(x_{max}),$$

that is, since $f(x_{max})$ occurs at $x_{max} = x_0$,

$$e^{-(x-x_0)^2/2\sigma^2} = \frac{1}{2} f(x_0) = \frac{1}{2}.$$

Solving we get

$$x_{\pm} = \pm\sqrt{2\ln 2} + x_0,$$

that is

$$FWHM \equiv x_+ - x_- = \sqrt{2\ln 2}\,\sigma = 2.3548\,\sigma.$$